



HAL
open science

Effects of Oxygen Fugacity on Hydroxyl Incorporation in Garnet at 1-3 GPa and 800-1000°C and Implications for Water Storage in the Mantle

Kai Zhang, Hanyong Liu, Dmitri A. Ionov, Xiaozhi Yang

► **To cite this version:**

Kai Zhang, Hanyong Liu, Dmitri A. Ionov, Xiaozhi Yang. Effects of Oxygen Fugacity on Hydroxyl Incorporation in Garnet at 1-3 GPa and 800-1000°C and Implications for Water Storage in the Mantle. *Journal of Geophysical Research: Solid Earth*, 2022, 127, 10.1029/2022JB023948 . insu-03668201

HAL Id: insu-03668201

<https://insu.hal.science/insu-03668201>

Submitted on 24 Mar 2023

HAL is a multi-disciplinary open access archive for the deposit and dissemination of scientific research documents, whether they are published or not. The documents may come from teaching and research institutions in France or abroad, or from public or private research centers.

L'archive ouverte pluridisciplinaire **HAL**, est destinée au dépôt et à la diffusion de documents scientifiques de niveau recherche, publiés ou non, émanant des établissements d'enseignement et de recherche français ou étrangers, des laboratoires publics ou privés.

Copyright

JGR Solid Earth

RESEARCH ARTICLE

10.1029/2022JB023948

Key Points:

- An experimental study of hydroxyl incorporation in garnet over a range of pressure, temperature, oxygen fugacity, and chemical composition
- The hydroxyl solubility in garnet under otherwise identical conditions is enhanced with decreasing oxygen fugacity
- The small hydroxyl storage capacity in peridotite garnet makes it unlikely a major water carrier in the mantle

Supporting Information:

Supporting Information may be found in the online version of this article.

Correspondence to:

X. Yang,
xzyang@nju.edu.cn

Citation:

Zhang, K., Liu, H., Ionov, D. A., & Yang, X. (2022). Effects of oxygen fugacity on hydroxyl incorporation in garnet at 1–3 GPa and 800–1000°C and implications for water storage in the mantle. *Journal of Geophysical Research: Solid Earth*, 127, e2022JB023948. <https://doi.org/10.1029/2022JB023948>

Received 6 JAN 2022
Accepted 23 MAR 2022

Effects of Oxygen Fugacity on Hydroxyl Incorporation in Garnet at 1–3 GPa and 800–1000°C and Implications for Water Storage in the Mantle

Kai Zhang¹ , Hanyong Liu¹, Dmitri A. Ionov² , and Xiaozhi Yang¹ 

¹State Key Laboratory for Mineral Deposits Research, School of Earth Sciences and Engineering, Nanjing University, Nanjing, China, ²Géosciences Montpellier, Université de Montpellier, Montpellier, France

Abstract Garnet, an important mineral component in Earth's interior, usually contains minor water as structural OH, but experimental data on OH incorporation in the mineral as a function of chemical and thermodynamic parameters remain rare. In particular, the role of oxygen fugacity (fO_2) that is variable in the Earth has not been well assessed. We examine the effects of fO_2 on the incorporation of OH at 1–3 GPa and 800–1000°C, by H-annealing gem-quality spessartine-rich, grossular-rich, and pyrope-rich garnets. For each type of annealed garnet, the OH peak positions and spectral shapes are the same, suggesting the same OH incorporation mechanism(s). Under identical conditions, spessartine-rich and grossular-rich garnets are rich in OH, with solubility orders of magnitudes greater than for pyrope-rich garnets. Over the studied conditions, the solubility of OH increases with pressure and temperature but decreases with fO_2 . The negative correlation of fO_2 and OH solubility is probably due to the Fe^{3+} to Fe^{2+} reduction at more reduced conditions and the coupled OH incorporation in the structure. The effects of fO_2 on OH solubility are more significant in Fe-rich garnets. The ascertained small OH solubility in peridotite garnets, together with comparisons with relevant studies, suggest that mantle garnet is unlikely to be a major water carrier. In combination with literature-reported positive correlation of fO_2 and OH solubility in olivine, the partition coefficient of OH between garnet and olivine in the upper mantle is expected to be redox-dependent.

Plain Language Summary The water incorporation in garnet is examined over a range of pressure, temperature, oxygen fugacity, and mineral chemistry, by conducting hydroxylation experiments with gem-quality natural crystals. Infrared absorption bands of structural water are observed in all annealed samples, and the water solubility under otherwise identical conditions is significantly different between different types of garnets. The incorporation mechanism of water in garnet is affected by factors other than the commonly assumed hydrogarnet substitution, and appears to be influenced also by magnesium and iron in the structure. The water solubility is enhanced with decreasing oxygen fugacity, and the increase is more significant in more Fe-rich garnets. The smaller water solubility in pyropes than previous estimates and the similarly low water storage capacity in peridotite garnets further suggest that garnet is not a major water carrier in the mantle.

1. Introduction

Garnet is an important mineral constituent of the deep continental crust, subducted oceanic crust, and upper mantle where garnet-bearing granulites, eclogites, peridotites, and pyroxenites are present. Studies on natural samples have shown that garnet often contains some structural OH groups ranging from several tens to thousands of ppm H_2O (Aines & Rossman, 1984; Bell & Rossman, 1992; Langer et al., 1993; Matsyuk et al., 1998; Rossman & Aines, 1991; Sheng et al., 2007; Xia et al., 2005). Therefore, garnet is important in understanding Earth's water budget. Laboratory experiments are crucial in assessing the incorporation of OH in garnet and its relation to factors such as pressure, temperature, fO_2 , and chemical composition. However, very few experiments have been performed for garnet, and the rare available work (Lu & Keppeler, 1997; Mookherjee & Karato, 2010; Withers et al., 1998) only assessed the effects of pressure and temperature on OH solubility.

fO_2 is a critical factor in describing Earth's redox state. It controls the valence state and speciation of key elements (e.g., H and Fe), the physicochemical nature of minerals and the style of interactions between different regions in the Earth and between Earth's interior and exterior. fO_2 is strongly variable in the Earth, both spatially and temporally. Relative to the fayalite-magnetite-quartz (FMQ) buffer, fO_2 is about FMQ – 2 to FMQ + 5 in the crust, FMQ – 1 to FMQ + 1 in the shallow mantle and FMQ – 4 to even more reduced below ~100–150 km depth, and the

mantle fO_2 has evolved from reduced conditions as low as $\sim FMQ - 6$ at shallow depths before ~ 4.0 Ga to more oxidized state today (Frost & McCammon, 2008; Goncharov et al., 2012; Stagno et al., 2013; Wood et al., 1990; Yang et al., 2014a). The OH storage in garnet may be affected by fO_2 , because it can change the relative proportions of Fe^{2+} and Fe^{3+} , thus the point-defect populations, and the relative partitioning of water between fluids (melts) and garnet. Significant and divergent effects of fO_2 on OH solubility have been documented for rutile (Colasanti et al., 2011), labradorite (Mosenfelder et al., 2020; Yang, 2012), olivine (Yang, 2016), and pyroxenes (Liu & Yang, 2020). The impact of fO_2 on OH incorporation in garnet should be characterized, however, this topic has not received much attention.

In this study, we examine the effects of fO_2 on the incorporation of OH in garnet, by performing annealing experiments at 1–3 GPa, 800–1,000°C. We use natural garnets (spessartine-rich, grossular-rich, and pyrope-rich), as well as a xenolith peridotite, as the starting materials. The annealing under otherwise identical conditions allows to put constraints on the incorporation mechanisms of OH in garnet and the OH solubility as a function of other factors. The data show that the OH solubility is enhanced under more reduced conditions, and the effects of fO_2 are more significant in Fe-rich garnets. In combination with relevant studies in available reports, the results are further applied to constrain the mantle water storage.

2. Experimental and Analytical Methods

2.1. Strategy

OH incorporation experiments at water-saturated conditions are usually regarded, for simplicity, as OH solubility experiments. Two approaches are often used. One is by growing mineral in a hydrous melt, obtained from a mixture of reagents (e.g., oxides) in stoichiometric proportions (experimental synthesis), and the other is by equilibrating natural or synthetic crystals with a hydrous fluid such as distilled water (experimental annealing). The latter has been widely applied to many minerals, for example, olivine (Bai & Kohlstedt, 1993; Kohlstedt et al., 1996; Mosenfelder et al., 2006; Yang, 2015, 2016; Yang et al., 2014b; Zhao et al., 2004), pyroxenes (Bromiley et al., 2004; Liu & Yang, 2020; Rauch & Keppeler, 2002), garnet (Lu & Keppeler, 1997; Mookherjee & Karato, 2010), feldspars (Behrens, 2021; Mosenfelder et al., 2020; Yang, 2012), quartz (Stalder et al., 2017), and rutile (Colasanti et al., 2011).

Both methods have advantages and disadvantages. The experimental synthesis can easily achieve equilibrium stoichiometry at run conditions. However, the grown grains are small, which is challenging for accurate water content analysis, and usually a very limited number of elements are added, for example, for the end-member mineral (note: the more elements added, the more complex the solid solutions and the more difficult the mineral growth). It is difficult to obtain minerals with major/minor elements matching those in terrestrial rocks, which affects OH incorporation (Berry et al., 2005; Rauch & Keppeler, 2002; Tollan et al., 2018). The experimental annealing can produce larger crystals with major/minor elements typical of natural materials, although the equilibrium is hard to reach at run conditions. This method is particularly useful to assess the effects of fO_2 , pressure or temperature on the incorporation of OH. For those experiments, the mineral chemistry is maintained unchanged, and the net effect of other factor(s) over a range of conditions is addressed. Crystals with different chemistry within a given mineral group can be used, for example, similar to synthesized samples doped with different elements to assess the chemical effects on OH incorporation under otherwise similar conditions, and a general link of OH solubility with a factor in interest is modeled. Using this approach, reaction rims between studied crystals and surrounding materials (e.g., pressure media or silica buffer) may form, as shown previously (Kohlstedt et al., 1996; Mosenfelder et al., 2006; Yang, 2015). The rims in most cases do not reach full equilibrium due to the sluggish exchange of Mg, Si or Fe, and are usually excluded from analysis. We use the latter approach for documenting the effects of fO_2 on OH incorporation in garnet, which is close to the classified M_2 method in Tollan et al. (2018) by equilibrating crystal point defects with H.

2.2. Starting Materials

The starting materials were natural gem-quality single crystals of garnet: an orange spessartine-rich crystal from Afghanistan (A6), a green grossular-rich crystal from Kenya (K2), a pink pyrope-rich crystal from Western Alps (D2) and several dark-red pyrope-rich crystals from Russia (U267 and U501). The garnets originated from the crust and mantle, but our results are unaffected, because the physicochemical properties of a mineral at

Table 1
Composition (wt. %) and Water Content (ppm H₂O) of Starting Garnets

	SiO ₂	TiO ₂	Al ₂ O ₃	Cr ₂ O ₃	FeO	MnO	MgO	CaO	NiO	Na ₂ O	K ₂ O	Total	ppm H ₂ O
Spessartine (A6)	35.21	0.02	20.55	<0.01	3.58	39.52	0.02	0.38	0.02	0.03	0.01	99.35	2,786
	<i>0.09</i>	<i>0.01</i>	<i>0.10</i>	<i>0.01</i>	<i>0.01</i>	<i>0.09</i>	<i>0.01</i>	<i>0.04</i>	<i>0.02</i>	<i>0.01</i>	<i>0.01</i>		
Grossular (K2)	39.95	0.42	21.44	0.07	0.07	0.72	0.55	36.30	<0.01	0.03	0.02	99.57	1,192
	<i>0.09</i>	<i>0.04</i>	<i>0.09</i>	<i>0.03</i>	<i>0.01</i>	<i>0.08</i>	<i>0.02</i>	<i>0.08</i>	<i>0.01</i>	<i>0.02</i>	<i>0.02</i>		
Pyrope (D2)	43.28	0.07	24.70	0.01	4.53	0.10	26.36	0.98	<0.01	<0.01	0.02	100.06	17
	<i>0.25</i>	<i>0.01</i>	<i>0.26</i>	<i>0.01</i>	<i>0.02</i>	<i>0.02</i>	<i>0.15</i>	<i>0.03</i>	<i>0.01</i>	<i>0.01</i>	<i>0.02</i>		
Pyrope (U267)	42.45	0.29	21.38	2.44	8.01	0.31	20.38	4.11	0.03	0.05	<0.01	99.47	16
	<i>0.02</i>	<i>0.01</i>	<i>0.05</i>	<i>0.02</i>	<i>0.07</i>	<i>0.01</i>	<i>0.11</i>	<i>0.01</i>	<i>0.03</i>	<i>0.01</i>	<i>0.01</i>		
Pyrope (U501)	41.47	0.23	19.73	5.15	8.49	0.48	18.60	5.25	0.02	0.03	<0.01	99.44	7
	<i>0.01</i>	<i>0.02</i>	<i>0.14</i>	<i>0.04</i>	<i>0.04</i>	<i>0.02</i>	<i>0.14</i>	<i>0.02</i>	<i>0.02</i>	<i>0.01</i>	<i>0.01</i>		

Note. Assuming all Fe as FeO, and data in the italic are the standard deviation. Uncertainty of H₂O contents is <2% for spessartine and grossular, and is mostly <7% for the three pyropes (see text).

fixed pressure, temperature, and chemical composition are independent of its origin. For simplicity, we use the end-member terms spessartine, grossular, and pyrope to refer to these garnets, as often used in similar studies (Geiger & Rossman, 2018; Lu & Keppler, 1997; Mookherjee & Karato, 2010). The pyropes are from the well-studied Dora Maira samples (Geiger & Rossman, 2018) and Udachnaya peridotites (Doucet et al., 2013, 2014; Ionov et al., 2010). Pyrope U267 and U501 were extracted from two peridotite xenoliths hosted by the Udachnaya kimberlite in the central Siberian craton, equilibrated at 5.4 GPa and 1,200°C (~FMQ – 2.7) and 4.8 GPa and 880°C (~FMQ – 2.9), respectively (Doucet et al., 2014; Ionov et al., 2010).

Starting crystals were 5–12 mm in size, except those from peridotites (0.5–1.5 mm). Kelyphite rims present on some peridotite garnets were removed by polishing. For each garnet, the crystals were chemically homogenous based on electron microprobe (EMP) analysis (Table 1). The initial OH content was 2,786 (A6), 1,192 (K2), 17 (D2), 16 (U267), and 7 (U501) ppm H₂O, measured by Fourier-transform infrared (FTIR) spectroscopy (Figure 1). Crystals were cut into 0.5 × 0.5 × 0.8 mm or smaller blocks, sometimes irregular in shape (peridotite garnets), for experimental runs. The crushed powder of a peridotite xenolith from North China, dominated by olivine and pyroxenes, was added to charges as pressure medium surrounding the blocks. Pyroxenes in the peridotite buffered

the silica activity to be a constant (Ardia et al., 2012; Bai & Kohlstedt, 1993; Kohlstedt et al., 1996; Liu & Yang, 2020; Mosenfelder et al., 2006). This method resembles the use of quartz as a silica activity buffer in studies of OH solubility in garnet (Lu & Keppler, 1997; Withers et al., 1998). The peridotite powder was used in all runs, so that for each garnet at a fixed pressure and temperature, the only experimental variable is *f*O₂ that makes the comparison of OH data of different garnet samples straightforward.

2.3. Experimental Studies

Experiments were carried out at 1–3 GPa and 800–1,000°C in an end-loaded piston cylinder press. A modified double-capsule technique was used, and *f*O₂ in the charges was imposed by the widely applied Fe₃O₄-Fe₂O₃ (HM), Ni-NiO (NNO) or Fe-FeO (IW) solid-state buffer pairs, which yield *f*O₂ ranging over 8–9 log units at a given pressure and temperature (NNO is close to FMQ, HM is ~NNO + 4 and IW is ~NNO – 4). Capsule design follows that in previous work (Liu & Yang, 2020; Yang, 2015, 2016; Yang et al., 2014b, 2016), and only a brief description is provided.

Thick-walled outer capsules were used, made of Pt, Ni, and Fe for *f*O₂ buffered by HM, NNO, and IW, respectively. For each run, 2–3 garnet blocks

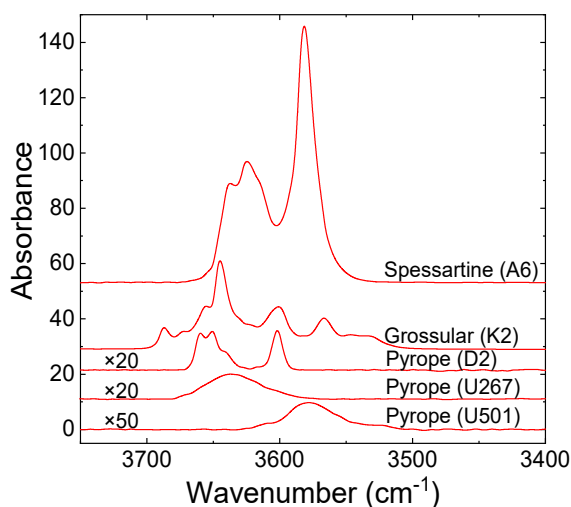


Figure 1. Fourier-transform infrared (FTIR) spectra of starting garnets. Intensity of pyrope D2, U267, and U501 was multiplied by 20, 20, and 50, respectively. Spectra were normalized to 1 cm thickness.

Table 2
Summary of Run Conditions and Equilibrium Fluid Compositions

	P (GPa)	T ($^{\circ}\text{C}$)	$f\text{O}_2$ buffer	Duration (h)	$\log f\text{O}_2$ (bar)	$f\text{H}_2\text{O}$ (bar)	$f\text{H}_2$ (bar)	$X(\text{H}_2\text{O})$	$X(\text{H}_2)$
B273	1	1,000	IW	40	-14.46	1.24E + 04	1.25E + 04	0.70	0.30
A198	1	1,000	NNO	40	-9.86	1.76E + 04	8.98E + 01	1.00	<0.01
A203	1	1,000	HM	40	-5.48	1.76E + 04	5.80E - 01	1.00	<0.01
B287	1.5	1,000	IW	40	-14.24	3.65E + 04	2.89E + 04	0.77	0.23
A208	1.5	1,000	NNO	40	-9.68	4.74E + 04	1.96E + 02	1.00	<0.01
A209	1.5	1,000	HM	40	-5.41	4.75E + 04	1.43E + 00	1.00	<0.01
B276	2	1,000	IW	40	-14.03	9.51E + 04	5.86E + 04	0.82	0.18
A199	2	1,000	NNO	40	-9.5	1.16E + 05	3.90E + 02	1.00	<0.01
A202	2	1,000	HM	40	-5.33	1.16E + 05	3.22E + 00	1.00	<0.01
B281	2	900	IW	80	-15.8	1.03E + 05	6.31E + 04	0.84	0.16
A205	2	900	NNO	80	-11.11	1.22E + 05	3.39E + 02	1.00	<0.01
A207	2	800	IW	140	-17.89	1.12E + 05	6.59E + 04	0.87	0.13
B283	2	800	NNO	140	-13.02	1.28E + 05	2.75E + 02	1.00	<0.01
B278	3	1,000	IW	40	-13.6	5.22E + 05	1.96E + 05	0.89	0.11
A200	3	1,000	NNO	40	-9.14	5.88E + 05	1.30E + 03	1.00	<0.01
A201	3	1,000	HM	40	-5.18	5.89E + 05	1.37E + 01	1.00	<0.01
A223	2	1,000	IW	40	-14.03	9.51E + 04	5.86E + 04	0.82	0.18
A222	2	1,000	NNO	40	-9.5	1.16E + 05	3.90E + 02	1.00	<0.01

Note. At a given pressure and temperature, NNO is 4–5 log units more oxidizing than IW, and HM is 4–5 log units more oxidizing than NNO. $f\text{O}_2$ was calculated from Frost (1991) and Herd (2008). $f\text{H}_2\text{O}$, $f\text{H}_2$, $X(\text{H}_2\text{O})$, and $X(\text{H}_2)$ are the equilibrium water and hydrogen fugacity and molar fraction of H_2O and H_2 in the runs, respectively, calculated by considering the dissociation of H_2O ($\text{H}_2\text{O} = \text{H}_2 + 0.5\text{O}_2$) and its equation of state (Zhang & Duan, 2009) and equilibrium constant (Robie & Hemingway, 1995). These parameters are linked to $f\text{O}_2$, P , and T , and are not independent in both the calculation and charges. Dissolution of silicate minerals in the fluids is not considered.

were each wrapped by a Au foil that can be treated as the inner capsule, and were then loaded into the outer capsule, along with peridotite powder, buffer oxide(s) and distilled water. Au foil was not sealed, and was used to protect the garnet crystals from serious reactions with other materials in the charge. Distilled water and buffer oxides (Fe_3O_4 - Fe_2O_3 , NiO or FeO) were placed at the bottom of the one-end sealed outer capsule, and were separated from the peridotite powder and garnet samples by a thin Pt foil. The amount of added distilled water was 2–3 wt. % in each charge. Pt capsules (ID 4.6 mm, OD 5 mm and length 10 mm) were sealed by arc welding, and Ni and Fe capsules (ID 4.2 mm, OD 5 mm, and length 10 mm) were sealed by mechanical compression in the press. Experiments used 0.75'' (1 GPa) and 0.5'' (1.5–3 GPa) assemblies, made of pyrophyllite, talc, Pyrex glass, graphite, and crushable alumina. Temperature was controlled by a type-S thermocouple, and fluctuation was usually within $\pm 1^{\circ}\text{C}$ in each run. Run durations were 40–140 hr, and were chosen by considering the grain sizes and H diffusivity of garnets, ensuring the equilibrium OH incorporation at the fixed sample composition while maintaining the survival of fluids and oxygen buffer pairs in the runs. The H diffusivity data of garnet were referred from the compilation of Ingrin and Blanchard (2006), and some extremely low diffusion data (including Reynes et al. (2018)), lower by 3 six orders of magnitude than the majority of the H diffusivity in Ingrin and Blanchard (2006), were not considered. A summary of the run conditions is given in Table 2.

We attempted to perform several experiments with the spessartine (A6), grossular (K2), and pyrope (D2) at 2 GPa and 1,050–1,200 $^{\circ}\text{C}$, but the garnets always decomposed. Some spessartines and pyropes annealed at 1 GPa and 1,000 $^{\circ}\text{C}$ decomposed as well. These runs are not shown in Table 2. At the end of each run, the samples were quenched to room temperature by powering off the heating circuit, and pressure was then released over 10–20 hr to minimize crystal fracturing. Recovered capsules were weighed and pierced, then heated and reweighed to test for the presence of water. Capsules that did not release excess water after the runs were discarded. The capsules were cut open, and the garnet crystals were carefully separated. In each capsule, the presence of oxygen

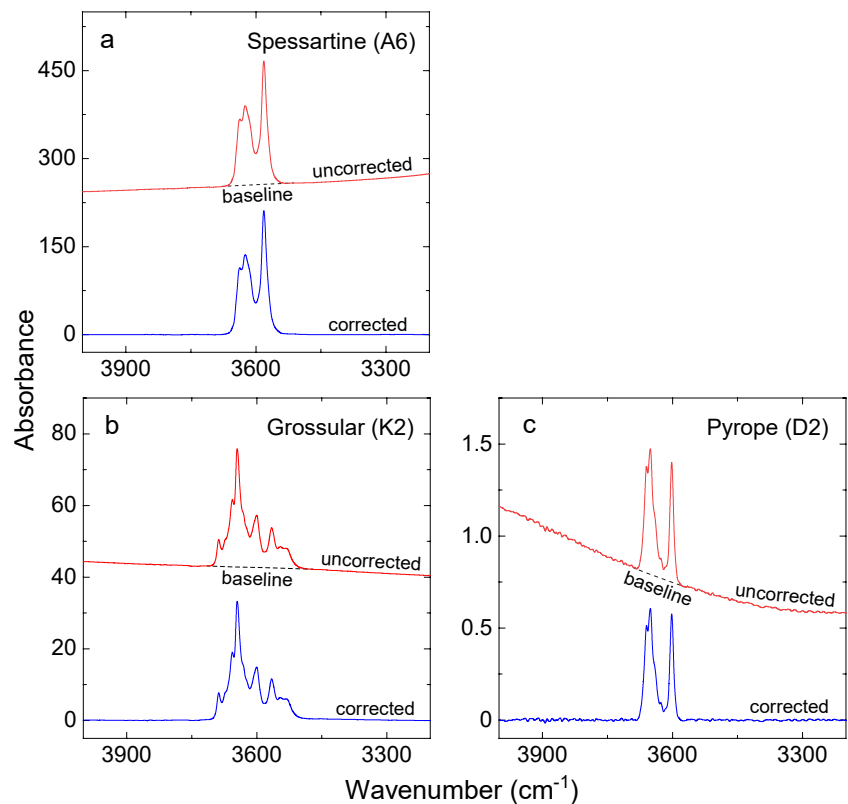


Figure 2. Baseline corrections of representative spectra. (a) Spessartine from A202, (b) grossular from A200, and (c) pyrope from A202. Spectra were normalized to 1 cm thickness.

buffer pairs was examined by optical or scanning electron microscopy. The textures of the peridotite, garnets and capsules were imaged by scanning electron microscopy, and the chemical composition of garnets was measured by EMP. The garnet crystals were polished for FTIR analyses. Thin reaction rims found on the crystals were not analyzed (see Section 2.1). Thickness of polished samples was 0.16–0.60 mm, as determined by a Mitutoyo digital micrometer.

2.4. Analytical Methods

Chemical composition was measured using a JEOL JXA-8230 EMP analyzer. The work conditions were: 15 kV accelerating voltage, 10 nA beam current, <5 μm beam size, and counting time of 10 and 5 s for the peak and background, respectively. Natural minerals and synthetic oxides were used as standards. The peridotite matrix and oxygen buffer pairs were examined with a field-emission TESCAN Mira3 scanning electron microscope.

The OH bands and contents were determined by FTIR spectroscopy. FTIR spectra were measured using a Bruker Vertex 70V spectrometer coupled to a Hyperion 2000 microscope: a global source, KBr/Ge beam-splitter, MCT detector, aperture of 60 × 60 μm, resolution of 4 cm⁻¹ and 128 scans for each spectrum. Unpolarized radiation was used for the cubic garnet. Optically clear zones, free of inclusions/cracks, were analyzed. Profile FTIR analyses were performed on representative crystals. A spline-fit method was used for spectral baseline corrections (Figure 2). Water content was obtained by the Beer-Lambert law, $C_{OH} = Abs_{tot}/I$, where C_{OH} is OH content (ppm H₂O), Abs_{tot} is the integral absorbance of OH bands at 3,700–3,500 cm⁻¹ (normalized to 1 cm thickness), and I is the mineral-specific integral molar absorption coefficient. Uncertainty of water content by baseline subtractions is <2% for the OH-rich spessartine and grossular where the baselines are easy to define, and is often <7% for the OH-poor pyropes where the baselines are easily subjected to weak noisy signals in the spectra. This is the arbitrary uncertainty by the manual processing of the spectra, evaluated by conducting several reasonable baseline fittings to a few representative spectra.

The garnet-specific integral calibration coefficient of Bell et al. (1995), $\sim 1.39 \text{ ppm}^{-1} \text{ cm}^{-2}$, was used to calculate the water content. Ideally, this calibration is applicable to garnets with similar OH bands as in Bell et al. (1995). A later report of Maldener et al. (2003), using nuclear reaction analysis and FTIR spectroscopy, has shown that, except some grossular samples dominated by high frequency OH bands ($3,680\text{--}3,645 \text{ cm}^{-1}$), the calibration coefficient of garnet is similar over a variety of mineral compositions and OH bands. A universal coefficient, $\sim 0.75 \text{ ppm}^{-1} \text{ cm}^{-2}$, was proposed for OH in garnet by Maldener et al. (2003), which is $\sim 50\%$ smaller than the one of Bell et al. (1995) and results in water contents greater by $\sim 50\%$. For grossular, the coefficient is $\sim 2.59 \text{ ppm}^{-1} \text{ cm}^{-2}$ in Maldener et al. (2003), that is confirmed by Reynes et al. (2018) and is similar to the $\sim 2.70 \text{ ppm}^{-1} \text{ cm}^{-2}$ in Mosenfelder et al. (2021). Applying these coefficients to our grossular samples leads to $\sim 50\%$ smaller water content relative to the method of Bell et al. (1995). OH contents obtained by applying these calibration coefficients are summarized in Table 3 (*Note.* for each type of garnet, the OH band positions are similar between our samples and those used for establishing the calibration coefficients). Our general results, in particular the effects of $f\text{O}_2$ on OH solubility that is determined by the relative variation of Abs_{OH} , are not affected by the choice of the coefficients. For simplicity, the water contents discussed below are based on the calibration of Bell et al. (1995).

3. Results

In each of the recovered capsules, no melt in the form of films, lens or pockets was observed on the exposed surface, either at the sides, bottom or top of the capsules or between mineral grains. This, along with the presence of excess water in the capsules, suggests the annealing under subsolidus and water-saturated conditions. The original shapes of the garnet crystals are usually preserved, although fractures appeared in most cases (Figure 3). No zoned distribution in recovered samples is observed for major/minor elements (Tables 4–7) and OH (Figure 4). In comparison with the starting materials (Table 1), the samples show no chemical changes during the experiments.

Typical FTIR spectra of annealed garnets are shown in Figure 5. The samples show OH absorption bands at $3,700\text{--}3,500 \text{ cm}^{-1}$. For each garnet, the frequencies and shapes of the OH bands in the annealed samples are essentially the same as those in the starting material (Figure 1). The OH bands are different between different garnets. In general, the spectra show the dominant bands at $3,637$, $3,624$, $3,615$, and $3,581 \text{ cm}^{-1}$ for spessartine, at $3,688$, $3,673$, $3,656$, $3,645$, $3,630$, $3,600$, $3,565$, $3,545$, and $3,531 \text{ cm}^{-1}$ for grossular, at $3,660$, $3,651$, $3,641$, $3,624$, $3,617$, and $3,601 \text{ cm}^{-1}$ for pyrope D2, at $3,637 \text{ cm}^{-1}$ for pyrope U267 and at $3,611$ and $3,578 \text{ cm}^{-1}$ for pyrope U501.

The H_2O content in the annealed samples is highly variable, for example, $5,830\text{--}7,750 \text{ ppm}$ in spessartine, $1,180\text{--}1,450 \text{ ppm}$ in grossular, and $10\text{--}30 \text{ ppm}$ in pyropes (Table 3). The content at comparable conditions is much lower, by a factor of up to ~ 770 , in pyropes than in spessartine and grossular (Figure 6). This variation is far beyond the ranges that can be produced by the difference in OH calibration coefficients between these garnets, as documented in Section 2.4. The OH content increases linearly with pressure (Figure 7) and temperature (Figure 8), but decreases linearly with $\log f\text{O}_2$ (Figure 9). For each garnet, the ratio of OH content at IW and at NNO under otherwise identical conditions, $C_{\text{OH}}^{\text{IW}}/C_{\text{OH}}^{\text{NNO}}$, is independent of run pressure and temperature in the experiments, as observed for spessartine (Figure 10a), grossular (Figure 10b), and pyrope D2 (Figure 10c). The average values of $C_{\text{OH}}^{\text{IW}}/C_{\text{OH}}^{\text{NNO}}$, if two or more ratios are available from the experiments, are ~ 1.07 , 1.05 , 1.29 , 2.20 , and 2.10 for the spessartine, grossular and pyropes D2, U267, and U501, respectively (Figure 10).

4. Comparison With Garnet OH in Other Studies

The general OH frequencies and band shapes in the annealed samples (Figure 5) are similar to those in previous studies on OH bands in matching types of natural (Aines & Rossman, 1984; Bell et al., 1995, 2004; Bell & Rossman, 1992; Doucet et al., 2014; Geiger & Rossman, 2018; Maldener et al., 2003; Matsyuk et al., 1998; Mosenfelder et al., 2021; Rossman & Aines, 1991) and annealed/synthetic (Lu & Keppler, 1997; Withers et al., 1998) garnets. The broad OH bands at $3,800\text{--}3,000 \text{ cm}^{-1}$ in a pyrope annealed at $5\text{--}9 \text{ GPa}$ and $1,100\text{--}1,200^\circ\text{C}$ by Mookherjee and Karato (2010) differ greatly from the narrow bands at $3,700\text{--}3,500 \text{ cm}^{-1}$ in pyropes obtained at $1\text{--}10 \text{ GPa}$ and $800\text{--}1,000^\circ\text{C}$ in other experiments (Lu & Keppler, 1997; Withers et al., 1998) and this study, and the reason for the contrast is still unclear. However, it should be noted that the OH bands are strongly variable in either megacryst or peridotite garnets of comparable composition (Bell et al., 2004; Doucet et al., 2014; Matsyuk et al., 1998).

Table 3
Water Content in Recovered Garnet Samples

	ppm H ₂ O ^a						ppm H ₂ O ^b						ppm H ₂ O ^c		ppm H ₂ O ^d										
	Spessartine (A6)		Grossular (K2)		Pyrope (D2)		Pyrope (U267)		Pyrope (U501)		Spessartine (A6)		Grossular (K2)		Pyrope (D2)		Pyrope (U267)		Pyrope (U501)		Grossular (K2)				
B273	-	1,376/1,351/1,333	-	-	-	-	-	-	-	-	-	-	-	-	-	-	-	-	-	-	-	-	738/725/715	708/696/686	
A198	-	1,312	-	-	-	-	-	-	-	-	-	-	-	-	-	-	-	-	-	-	-	-	704	675	
A203	-	1,247/1,258	-	-	-	-	-	-	-	-	-	-	-	-	-	-	-	-	-	-	-	-	669/675	642/648	
B287	7,154/7,107	1,357/1,376	25/26	13,259/13,172	2,515/2,550	46/48	12,423	2,463	35/37	684	728/738	699/708	713	684	676/690	649/662	749/757	709/731	681/701	658/668	700	672	665/660	638/633	
A208	6,703	1,329	19/20	11,783	2,335/2,382	28/30	11,783	2,450/2,524	37/39	682	634	608	781/763	750/732	733/749/741	703/719/710	716/703	687/674	41	39	19	19	19	19	
A209	6,358	1,260/1,285	15/16	13,700/13,757	2,587/2,613	52/50/50	13,700/13,757	2,450/2,524	30/30	13,403/13,311/13,479	2,532/2,587/2,558	43/44	32/33	32/33	32/33	32/33	32/33	32/33	32/33	32/33	32/33	32/33	32/33	32/33	32/33
B276	7,392/7,423	1,396/1,410	28/27/27	12,106	2,369/2,404	30/30	12,106	2,369/2,404	30/30	12,399	2,472/2,426	32/33	32/33	32/33	32/33	32/33	32/33	32/33	32/33	32/33	32/33	32/33	32/33	32/33	32/33
A199	6,984/7,024/6,912	1,322/1,362	20/21	12,706/12,875	2,419	41/39	12,706/12,875	2,419	41/39	12,399	2,472/2,426	32/33	32/33	32/33	32/33	32/33	32/33	32/33	32/33	32/33	32/33	32/33	32/33	32/33	32/33
A202	6,532	1,278/1,297	16/16	11,743/11,872	2,298/2,280	32/32	11,743/11,872	2,298/2,280	32/32	11,837/11,769	2,356	33	33	33	33	33	33	33	33	33	33	33	33	33	33
B281	6,856/6,947	1,305	22/21	10,809/10,669	2,189	24/26	10,809/10,669	2,189	24/26	10,809/10,669	2,189	24/26	24/26	24/26	24/26	24/26	24/26	24/26	24/26	24/26	24/26	24/26	24/26	24/26	24/26
A205	6,336/6,406	1,240/1,230	17/17	14,367/14,296	2,698/2,635	54/57	14,367/14,296	2,698/2,635	54/57	14,403/13,311/13,479	2,532/2,587/2,558	43/44	43/44	43/44	43/44	43/44	43/44	43/44	43/44	43/44	43/44	43/44	43/44	43/44	43/44
A207	6,387/6,350	1,271	18	13,403/13,311/13,479	2,532/2,587/2,558	43/44	13,403/13,311/13,479	2,532/2,587/2,558	43/44	13,403/13,311/13,479	2,532/2,587/2,558	43/44	43/44	43/44	43/44	43/44	43/44	43/44	43/44	43/44	43/44	43/44	43/44	43/44	43/44
B283	5,832/5,757	1,181	13/14	13,403/13,311/13,479	2,532/2,587/2,558	43/44	13,403/13,311/13,479	2,532/2,587/2,558	43/44	13,403/13,311/13,479	2,532/2,587/2,558	43/44	43/44	43/44	43/44	43/44	43/44	43/44	43/44	43/44	43/44	43/44	43/44	43/44	43/44
B278	7,752/7,714	1,456/1,422	29/31	13,403/13,311/13,479	2,532/2,587/2,558	43/44	13,403/13,311/13,479	2,532/2,587/2,558	43/44	13,403/13,311/13,479	2,532/2,587/2,558	43/44	43/44	43/44	43/44	43/44	43/44	43/44	43/44	43/44	43/44	43/44	43/44	43/44	43/44
A200	7,232/7,182/7,273	1,366/1,396/1,380	23/24	13,403/13,311/13,479	2,532/2,587/2,558	43/44	13,403/13,311/13,479	2,532/2,587/2,558	43/44	13,403/13,311/13,479	2,532/2,587/2,558	43/44	43/44	43/44	43/44	43/44	43/44	43/44	43/44	43/44	43/44	43/44	43/44	43/44	43/44
A201	6,690	1,334/1,309	17/18	13,403/13,311/13,479	2,532/2,587/2,558	43/44	13,403/13,311/13,479	2,532/2,587/2,558	43/44	13,403/13,311/13,479	2,532/2,587/2,558	43/44	43/44	43/44	43/44	43/44	43/44	43/44	43/44	43/44	43/44	43/44	43/44	43/44	43/44
A223				22	21	10	22	21	10	22	21	10	22	21	10	22	21	10	22	21	10	22	21	10	22
A222				10	10	10	10	10	10	10	10	10	10	10	10	10	10	10	10	10	10	10	10	10	10

Note. →, garnet decomposed. Uncertainty of H₂O contents is <2% for spessartine and grossular, and is mostly <7% for the three pyropes (see text).
^aCalculated with the pyrope calibration coefficient of Bell et al. (1995). ^bCalculated with the universal calibration coefficient of Maldener et al. (2003). ^cCalculated with the grossular calibration coefficient of Maldener et al. (2003). ^dCalculated with the grossular calibration coefficient of Mosenfelder et al. (2021).

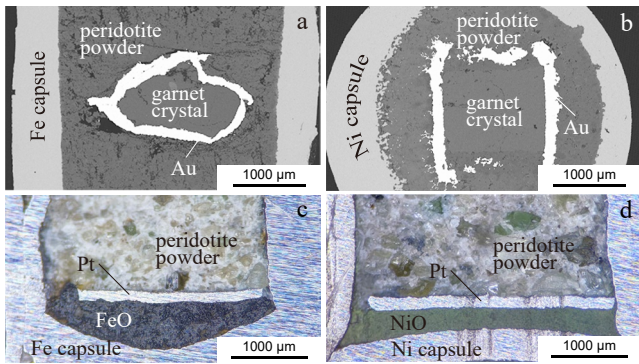


Figure 3. Representative recovered samples. (a) A pyrope crystal in peridotite from B278. (b) A grossular crystal in peridotite from A198, (c) FeO located at one end of the Fe capsule and separated by a Pt foil from the peridotite from B281, and (d) NiO located at one end of the Ni capsule and separated by a Pt foil from the peridotite from A205.

Despite the enhanced peak intensity after the experiments, the annealing obviously did not change the peak positions and spectral shapes of OH bands in each of the studied garnets (Figures 1 and 5), which has also been reported for pyropes by Lu and Keppler (1997) and Withers et al. (1998). This suggests the OH incorporation by decorating preexisting point defects with H (Tollan et al., 2018), driven mainly by H diffusion into the lattice and related substitutions. This, however, does not imply that the experimental method (Section 2.1) affected the OH bands in the annealed samples. In fact, it has been shown that, if major/minor elements and environmental factors (silica buffer and water source materials) are comparable, the general OH patterns of a mineral are consistent for growing crystals from a hydrous melt and equilibrating natural crystals with a hydrous fluid, as shown for olivine (Berry et al., 2005; Yang, 2015, 2016; Yang & Keppler, 2011; Yang et al., 2014b) and pyroxenes (Rauch & Keppler, 2002). Hence, the contrasting OH bands in different garnets are assigned to their different compositions, which affected the local crystal configurations and point defects (and OH substitutions).

Table 4
Composition of Recovered Spessartine Samples Starting With A6 (wt. %)

	SiO ₂	TiO ₂	Al ₂ O ₃	Cr ₂ O ₃	FeO	MnO	MgO	CaO	NiO	Na ₂ O	K ₂ O	Total
A209	34.43	0.03	20.63	<0.01	3.38	40.22	<0.01	0.43	0.04	0.01	<0.01	99.16
	<i>0.16</i>	<i>0.01</i>	<i>0.12</i>	<i>0.01</i>	<i>0.01</i>	<i>0.10</i>	<i>0.01</i>	<i>0.02</i>	<i>0.01</i>	<i>0.01</i>	<i>0.01</i>	
B287	34.81	0.06	20.60	0.02	3.50	39.88	<0.01	0.40	0.03	0.03	<0.01	99.33
	<i>0.09</i>	<i>0.02</i>	<i>0.01</i>	<i>0.01</i>	<i>0.01</i>	<i>0.11</i>	<i>0.01</i>	<i>0.03</i>	<i>0.03</i>	<i>0.01</i>	<i>0.01</i>	
A208	35.07	0.07	20.45	0.03	3.44	40.08	<0.01	0.41	<0.01	<0.01	<0.01	99.55
	<i>0.14</i>	<i>0.01</i>	<i>0.15</i>	<i>0.01</i>	<i>0.06</i>	<i>0.23</i>	<i>0.01</i>	<i>0.02</i>	<i>0.01</i>	<i>0.01</i>	<i>0.01</i>	
A202	35.25	0.05	20.72	<0.01	3.51	39.90	<0.01	0.41	0.07	0.02	<0.01	99.94
	<i>0.01</i>	<i>0.01</i>	<i>0.08</i>	<i>0.01</i>	<i>0.02</i>	<i>0.38</i>	<i>0.01</i>	<i>0.01</i>	<i>0.07</i>	<i>0.01</i>	<i>0.01</i>	
B276	35.19	<0.01	20.73	<0.01	3.49	39.45	<0.01	0.37	<0.01	0.02	<0.01	99.25
	<i>0.16</i>	<i>0.01</i>	<i>0.01</i>	<i>0.01</i>	<i>0.01</i>	<i>0.06</i>	<i>0.01</i>	<i>0.02</i>	<i>0.01</i>	<i>0.02</i>	<i>0.01</i>	
A199	35.44	0.01	20.73	<0.01	3.50	39.68	0.01	0.40	<0.01	0.04	<0.01	99.81
	<i>0.02</i>	<i>0.01</i>	<i>0.20</i>	<i>0.01</i>	<i>0.04</i>	<i>0.10</i>	<i>0.01</i>	<i>0.02</i>	<i>0.01</i>	<i>0.01</i>	<i>0.01</i>	
A207	34.49	0.04	20.41	<0.01	3.55	39.65	<0.01	0.44	0.11	<0.01	<0.01	98.69
	<i>0.02</i>	<i>0.03</i>	<i>0.02</i>	<i>0.01</i>	<i>0.06</i>	<i>0.15</i>	<i>0.01</i>	<i>0.01</i>	<i>0.04</i>	<i>0.01</i>	<i>0.01</i>	
B283	34.74	0.02	20.29	<0.01	3.44	39.69	<0.01	0.42	<0.01	0.04	<0.01	98.63
	<i>0.07</i>	<i>0.02</i>	<i>0.05</i>	<i>0.01</i>	<i>0.01</i>	<i>0.09</i>	<i>0.01</i>	<i>0.01</i>	<i>0.01</i>	<i>0.01</i>	<i>0.01</i>	
B281	35.03	0.04	20.68	0.02	3.51	40.20	0.02	0.39	<0.01	0.01	<0.01	99.90
	<i>0.07</i>	<i>0.03</i>	<i>0.17</i>	<i>0.01</i>	<i>0.04</i>	<i>0.10</i>	<i>0.01</i>	<i>0.01</i>	<i>0.01</i>	<i>0.01</i>	<i>0.01</i>	
A205	35.02	0.04	20.65	0.01	3.54	40.30	0.02	0.38	<0.01	<0.01	<0.01	99.95
	<i>0.10</i>	<i>0.01</i>	<i>0.05</i>	<i>0.01</i>	<i>0.01</i>	<i>0.12</i>	<i>0.01</i>	<i>0.03</i>	<i>0.01</i>	<i>0.01</i>	<i>0.01</i>	
A201	34.75	0.04	20.31	0.03	3.41	39.60	<0.01	0.39	<0.01	0.02	<0.01	98.53
	<i>0.02</i>	<i>0.04</i>	<i>0.01</i>	<i>0.01</i>	<i>0.01</i>	<i>0.02</i>	<i>0.01</i>	<i>0.06</i>	<i>0.01</i>	<i>0.01</i>	<i>0.01</i>	
B278	35.34	0.01	20.55	<0.01	3.49	39.93	0.01	0.38	0.03	0.03	<0.01	99.78
	<i>0.06</i>	<i>0.01</i>	<i>0.03</i>	<i>0.01</i>	<i>0.02</i>	<i>0.10</i>	<i>0.01</i>	<i>0.01</i>	<i>0.03</i>	<i>0.01</i>	<i>0.01</i>	
A200	34.70	0.03	20.46	<0.01	3.53	39.75	0.02	0.37	<0.01	0.03	<0.01	98.88
	<i>0.01</i>	<i>0.02</i>	<i>0.16</i>	<i>0.01</i>	<i>0.03</i>	<i>0.03</i>	<i>0.01</i>	<i>0.03</i>	<i>0.01</i>	<i>0.01</i>	<i>0.01</i>	

Note. Assuming all Fe as FeO, and data in the italic are the standard deviation.

Table 5

Composition of Recovered Grossular Samples Starting With K2 (wt. %)

	SiO ₂	TiO ₂	Al ₂ O ₃	Cr ₂ O ₃	FeO	MnO	MgO	CaO	NiO	Na ₂ O	K ₂ O	Total
A209	39.51	0.32	22.16	0.04	0.05	0.68	0.55	36.37	0.02	0.02	<0.01	99.72
	<i>0.36</i>	<i>0.05</i>	<i>0.06</i>	<i>0.02</i>	<i>0.01</i>	<i>0.02</i>	<i>0.03</i>	<i>0.07</i>	<i>0.02</i>	<i>0.01</i>	<i>0.01</i>	
B287	39.58	0.36	22.15	0.09	0.09	0.71	0.53	36.27	0.03	0.01	<0.01	99.84
	<i>0.12</i>	<i>0.02</i>	<i>0.01</i>	<i>0.02</i>	<i>0.02</i>	<i>0.01</i>	<i>0.02</i>	<i>0.16</i>	<i>0.01</i>	<i>0.01</i>	<i>0.01</i>	
A208	39.62	0.39	22.26	0.08	0.08	0.69	0.50	35.94	0.06	0.03	<0.01	99.63
	<i>0.09</i>	<i>0.01</i>	<i>0.10</i>	<i>0.02</i>	<i>0.01</i>	<i>0.02</i>	<i>0.01</i>	<i>0.16</i>	<i>0.06</i>	<i>0.01</i>	<i>0.01</i>	
A203	39.60	0.46	21.77	0.06	0.11	0.69	0.58	36.31	0.04	<0.01	0.02	99.65
	<i>0.34</i>	<i>0.02</i>	<i>0.02</i>	<i>0.01</i>	<i>0.01</i>	<i>0.01</i>	<i>0.01</i>	<i>0.11</i>	<i>0.04</i>	<i>0.01</i>	<i>0.01</i>	
B273	39.48	0.40	21.67	0.08	0.07	0.64	0.58	36.41	<0.01	<0.01	<0.01	99.33
	<i>0.07</i>	<i>0.01</i>	<i>0.23</i>	<i>0.01</i>	<i>0.01</i>	<i>0.04</i>	<i>0.02</i>	<i>0.31</i>	<i>0.01</i>	<i>0.01</i>	<i>0.01</i>	
A198	39.46	0.38	21.62	0.02	0.10	0.67	0.54	36.35	<0.01	<0.01	0.01	99.15
	<i>0.20</i>	<i>0.01</i>	<i>0.13</i>	<i>0.02</i>	<i>0.03</i>	<i>0.01</i>	<i>0.01</i>	<i>0.25</i>	<i>0.01</i>	<i>0.01</i>	<i>0.01</i>	
A202	39.66	0.39	22.30	0.04	0.07	0.67	0.57	35.75	0.12	0.02	<0.01	99.60
	<i>0.16</i>	<i>0.01</i>	<i>0.01</i>	<i>0.03</i>	<i>0.04</i>	<i>0.01</i>	<i>0.02</i>	<i>0.06</i>	<i>0.03</i>	<i>0.02</i>	<i>0.01</i>	
B276	40.04	0.40	22.24	0.04	0.08	0.69	0.59	36.24	0.11	<0.01	0.02	100.45
	<i>0.09</i>	<i>0.01</i>	<i>0.20</i>	<i>0.02</i>	<i>0.04</i>	<i>0.02</i>	<i>0.01</i>	<i>0.17</i>	<i>0.05</i>	<i>0.01</i>	<i>0.01</i>	
A199	39.94	0.34	22.21	0.04	0.06	0.68	0.57	36.08	0.02	0.02	<0.01	99.96
	<i>0.04</i>	<i>0.02</i>	<i>0.08</i>	<i>0.03</i>	<i>0.02</i>	<i>0.07</i>	<i>0.03</i>	<i>0.23</i>	<i>0.02</i>	<i>0.02</i>	<i>0.01</i>	
A207	39.78	0.40	22.08	0.07	0.06	0.72	0.56	35.89	0.05	<0.01	<0.01	99.63
	<i>0.10</i>	<i>0.02</i>	<i>0.05</i>	<i>0.01</i>	<i>0.03</i>	<i>0.04</i>	<i>0.01</i>	<i>0.04</i>	<i>0.03</i>	<i>0.01</i>	<i>0.01</i>	
B283	39.86	0.42	22.25	0.08	0.07	0.70	0.53	36.00	0.06	<0.01	<0.01	99.97
	<i>0.16</i>	<i>0.01</i>	<i>0.10</i>	<i>0.01</i>	<i>0.04</i>	<i>0.01</i>	<i>0.01</i>	<i>0.24</i>	<i>0.06</i>	<i>0.01</i>	<i>0.01</i>	
B281	39.63	0.36	22.13	0.03	0.07	0.64	0.56	36.04	0.16	<0.01	<0.01	99.62
	<i>0.16</i>	<i>0.02</i>	<i>0.10</i>	<i>0.02</i>	<i>0.06</i>	<i>0.01</i>	<i>0.01</i>	<i>0.21</i>	<i>0.06</i>	<i>0.01</i>	<i>0.01</i>	
A205	39.68	0.33	22.27	0.08	0.03	0.64	0.54	36.25	0.07	<0.01	0.02	99.93
	<i>0.04</i>	<i>0.01</i>	<i>0.17</i>	<i>0.01</i>	<i>0.01</i>	<i>0.04</i>	<i>0.01</i>	<i>0.01</i>	<i>0.04</i>	<i>0.01</i>	<i>0.02</i>	
A201	39.82	0.41	22.42	0.06	0.07	0.64	0.53	36.52	0.02	<0.01	<0.01	100.49
	<i>0.15</i>	<i>0.01</i>	<i>0.06</i>	<i>0.02</i>	<i>0.04</i>	<i>0.01</i>	<i>0.01</i>	<i>0.19</i>	<i>0.02</i>	<i>0.01</i>	<i>0.01</i>	
B278	39.27	0.37	22.28	0.05	0.05	0.66	0.56	36.51	<0.01	<0.01	<0.01	99.74
	<i>0.04</i>	<i>0.04</i>	<i>0.18</i>	<i>0.01</i>	<i>0.04</i>	<i>0.03</i>	<i>0.02</i>	<i>0.01</i>	<i>0.01</i>	<i>0.01</i>	<i>0.01</i>	
A200	39.41	0.41	22.42	0.04	0.08	0.69	0.54	36.13	0.09	0.01	0.01	99.84
	<i>0.23</i>	<i>0.05</i>	<i>0.09</i>	<i>0.01</i>	<i>0.03</i>	<i>0.06</i>	<i>0.01</i>	<i>0.28</i>	<i>0.07</i>	<i>0.02</i>	<i>0.01</i>	

Note. Assuming all Fe as FeO, and data in the italic are the standard deviation.

For the studied samples, the equilibrium OH solubility at a fixed mineral chemistry is supported by kinetic analyses of crystal sizes and H diffusivity in garnet (Section 2.3) and profile FTIR analyses of annealed crystals (Figure 4). The OH contents are greater in the annealed than in the corresponding starting garnets (Table 3). This is because natural minerals usually form at water-undersaturated conditions while the annealing runs are at water-saturated conditions. In NNO buffered runs, the OH solubility in pyrope D2 is 13–24 ppm, lower than the 70–100 ppm in Lu and Keppler (1997) for a Dora Maira pyrope of similar composition and 140–550 ppm in Withers et al. (1998) for a synthetic pyrope with unbuffered fO_2 . Besides, the negative correlation of OH content and fO_2 , generally observed for spessartine, grossular and pyrope (Figure 9) despite their different chemistry, contrasts with the positive trend at IW and NNO (2 GPa–1,000°C and 3 GPa–1,000°C) in Lu and Keppler (1997) for pyrope. Lu and Keppler (1997) and Withers et al. (1998) used quartz to buffer silica activity, in contrast to

Table 6
Composition of Recovered Pyrope Samples Starting With D2 (wt. %)

	SiO ₂	TiO ₂	Al ₂ O ₃	Cr ₂ O ₃	FeO	MnO	MgO	CaO	NiO	Na ₂ O	K ₂ O	Total
A209	43.01	0.02	24.58	0.01	4.87	0.06	25.77	0.86	<0.01	0.04	<0.01	99.22
	<i>0.19</i>	<i>0.02</i>	<i>0.11</i>	<i>0.01</i>	<i>0.02</i>	<i>0.01</i>	<i>0.01</i>	<i>0.06</i>	<i>0.01</i>	<i>0.02</i>	<i>0.01</i>	
B287	43.05	0.05	24.53	<0.01	4.83	0.05	25.95	0.89	0.05	0.02	<0.01	99.41
	<i>0.04</i>	<i>0.01</i>	<i>0.40</i>	<i>0.01</i>	<i>0.17</i>	<i>0.01</i>	<i>0.18</i>	<i>0.01</i>	<i>0.05</i>	<i>0.01</i>	<i>0.01</i>	
A208	43.32	0.01	24.64	<0.01	5.07	0.09	26.27	0.84	<0.01	0.06	0.02	100.33
	<i>0.12</i>	<i>0.01</i>	<i>0.06</i>	<i>0.01</i>	<i>0.04</i>	<i>0.03</i>	<i>0.25</i>	<i>0.06</i>	<i>0.01</i>	<i>0.01</i>	<i>0.02</i>	
A202	43.31	0.04	25.02	<0.01	4.48	0.09	26.10	1.06	0.02	0.04	0.01	100.17
	<i>0.43</i>	<i>0.01</i>	<i>0.29</i>	<i>0.01</i>	<i>0.03</i>	<i>0.05</i>	<i>0.12</i>	<i>0.14</i>	<i>0.02</i>	<i>0.02</i>	<i>0.01</i>	
B276	43.05	<0.01	24.89	0.02	4.69	0.10	26.64	0.69	<0.01	0.02	<0.01	100.09
	<i>0.36</i>	<i>0.01</i>	<i>0.17</i>	<i>0.01</i>	<i>0.06</i>	<i>0.02</i>	<i>0.10</i>	<i>0.06</i>	<i>0.01</i>	<i>0.02</i>	<i>0.01</i>	
A199	43.66	0.04	25.33	<0.01	4.51	0.06	26.31	0.77	0.03	0.06	<0.01	100.77
	<i>0.22</i>	<i>0.03</i>	<i>0.01</i>	<i>0.01</i>	<i>0.02</i>	<i>0.05</i>	<i>0.03</i>	<i>0.03</i>	<i>0.03</i>	<i>0.03</i>	<i>0.01</i>	
A207	42.58	0.02	24.39	<0.01	5.00	0.06	25.84	0.98	0.09	0.06	<0.01	99.02
	<i>0.10</i>	<i>0.03</i>	<i>0.01</i>	<i>0.01</i>	<i>0.08</i>	<i>0.03</i>	<i>0.03</i>	<i>0.02</i>	<i>0.01</i>	<i>0.01</i>	<i>0.01</i>	
B283	42.73	<0.01	24.75	<0.01	4.45	0.08	26.30	0.84	<0.01	0.05	<0.01	99.20
	<i>0.23</i>	<i>0.01</i>	<i>0.27</i>	<i>0.01</i>	<i>0.07</i>	<i>0.01</i>	<i>0.11</i>	<i>0.07</i>	<i>0.01</i>	<i>0.02</i>	<i>0.01</i>	
B281	43.09	0.06	24.50	<0.01	4.79	0.06	26.55	0.84	<0.01	0.05	<0.01	99.94
	<i>0.27</i>	<i>0.01</i>	<i>0.12</i>	<i>0.01</i>	<i>0.03</i>	<i>0.03</i>	<i>0.21</i>	<i>0.01</i>	<i>0.01</i>	<i>0.01</i>	<i>0.01</i>	
A205	43.28	<0.01	24.53	<0.01	4.76	0.07	26.48	0.83	<0.01	0.04	0.02	100.02
	<i>0.08</i>	<i>0.01</i>	<i>0.01</i>	<i>0.01</i>	<i>0.02</i>	<i>0.02</i>	<i>0.01</i>	<i>0.01</i>	<i>0.01</i>	<i>0.02</i>	<i>0.02</i>	
A201	42.81	0.04	24.36	0.03	4.51	0.05	26.39	0.90	<0.01	0.03	<0.01	99.10
	<i>0.13</i>	<i>0.01</i>	<i>0.01</i>	<i>0.01</i>	<i>0.02</i>	<i>0.03</i>	<i>0.27</i>	<i>0.05</i>	<i>0.01</i>	<i>0.01</i>	<i>0.01</i>	
B278	43.07	0.05	24.86	0.02	4.98	0.05	26.16	1.05	<0.01	0.05	<0.01	100.29
	<i>0.15</i>	<i>0.01</i>	<i>0.14</i>	<i>0.02</i>	<i>0.03</i>	<i>0.03</i>	<i>0.06</i>	<i>0.06</i>	<i>0.01</i>	<i>0.02</i>	<i>0.01</i>	
A200	43.29	<0.01	24.56	<0.01	4.25	0.08	26.63	0.67	0.05	0.01	<0.01	99.55
	<i>0.30</i>	<i>0.01</i>	<i>0.01</i>	<i>0.01</i>	<i>0.07</i>	<i>0.05</i>	<i>0.11</i>	<i>0.01</i>	<i>0.02</i>	<i>0.01</i>	<i>0.01</i>	

Note. Assuming all Fe as FeO, and data in the italic are the standard deviation.

Table 7
Composition of Recovered Pyrope Samples Starting With U267 and U501 (wt. %)

	SiO ₂	TiO ₂	Al ₂ O ₃	Cr ₂ O ₃	FeO	MnO	MgO	CaO	NiO	Na ₂ O	K ₂ O	Total
<i>Starting with U267</i>												
A222	42.64	0.29	21.22	2.49	8.01	0.28	20.92	4.18	0.02	0.05	<0.01	100.08
	<i>0.07</i>	<i>0.04</i>	<i>0.08</i>	<i>0.01</i>	<i>0.02</i>	<i>0.01</i>	<i>0.12</i>	<i>0.06</i>	<i>0.02</i>	<i>0.01</i>	<i>0.01</i>	
A223	42.66	0.27	21.59	2.56	7.93	0.32	20.90	4.15	<0.01	0.05	<0.01	100.43
	<i>0.01</i>	<i>0.01</i>	<i>0.19</i>	<i>0.06</i>	<i>0.03</i>	<i>0.01</i>	<i>0.03</i>	<i>0.02</i>	<i>0.01</i>	<i>0.01</i>	<i>0.01</i>	
<i>Starting with U501</i>												
A222	41.71	0.28	19.84	4.99	8.51	0.47	18.93	5.22	0.03	0.05	<0.01	100.02
	<i>0.11</i>	<i>0.01</i>	<i>0.06</i>	<i>0.09</i>	<i>0.04</i>	<i>0.01</i>	<i>0.03</i>	<i>0.01</i>	<i>0.01</i>	<i>0.01</i>	<i>0.01</i>	
A223	41.41	0.22	19.53	5.31	8.50	0.49	18.78	5.27	<0.01	0.02	<0.01	99.53
	<i>0.07</i>	<i>0.01</i>	<i>0.02</i>	<i>0.08</i>	<i>0.01</i>	<i>0.01</i>	<i>0.06</i>	<i>0.05</i>	<i>0.01</i>	<i>0.01</i>	<i>0.01</i>	

Note. Assuming all Fe as FeO, and data in the italic are the standard deviation.

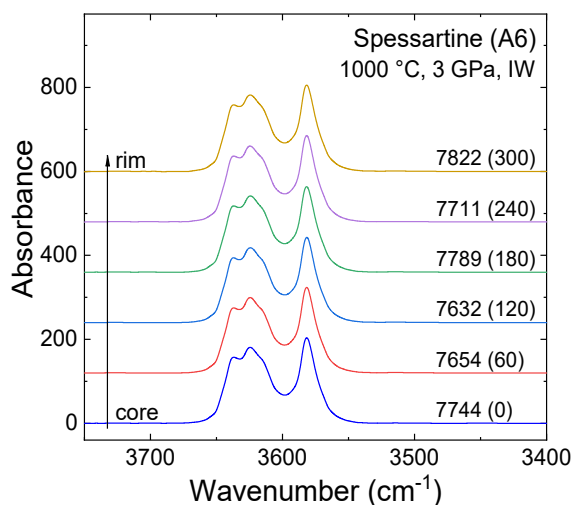


Figure 4. A typical Fourier-transform infrared (FTIR) profile of a spessartine crystal from A278. Numbers above each spectrum are integral absorbance (cm^{-2}) and distance from crystal center (μm in parentheses). Spectra were normalized to 1 cm thickness.

pyroxenes in this study, and the simple quartz + garnet assemblages in their runs differ from the complex peridotite minerals + garnet in ours. This may explain the different results in these studies, as demonstrated for olivine (e.g., Ardia et al., 2012; Yang, 2015, 2016; Yang et al., 2014b).

The increase in OH solubility with pressure at 1–3 GPa or temperature at 800–1,000°C is similar to that reported in Lu and Keppler (1997) and Withers et al. (1998). At subsolidus conditions, similar trends have been observed for olivine (Kohlstedt et al., 1996; Mosenfelder et al., 2006; Yang, 2016) and pyroxenes (Bromiley et al., 2004; Liu & Yang, 2020; Rauch & Keppler, 2002). This reflects the enhanced OH incorporation in minerals as pressure/temperature increases. If melt is present in the system, OH content can decrease with temperature, as reported for olivine (Ardia et al., 2012), which is due to reduced water activity and strong water partitioning into melt at higher temperature. The linear correlation trends of OH content with pressure (Figure 7), temperature (Figure 8), and $f\text{O}_2$ (Figure 9) are the apparent best data fits over the run conditions, and may not hold at greater ranges of these parameters. However, the general trends should not change, and the discussion on the effects of $f\text{O}_2$ on OH incorporation is unaffected (Section 2.1).

5. Complexity of OH Incorporation Mechanisms in Garnet

Extensive work on OH incorporation modes in garnets has been done by studying OH in natural and synthetic samples (Ackermann et al., 1983; Aines & Rossman, 1984; Geiger & Rossman, 2018, 2020a, 2020b; Lager et al., 1989; Matsyuk et al., 1998; Rossman & Aines, 1991). However, it remains poorly understood how trace amounts of OH are stored. The hydrogarnet cluster model, by four H^+ replacing a Si^{4+} , is often considered as the principal OH incorporation mechanism

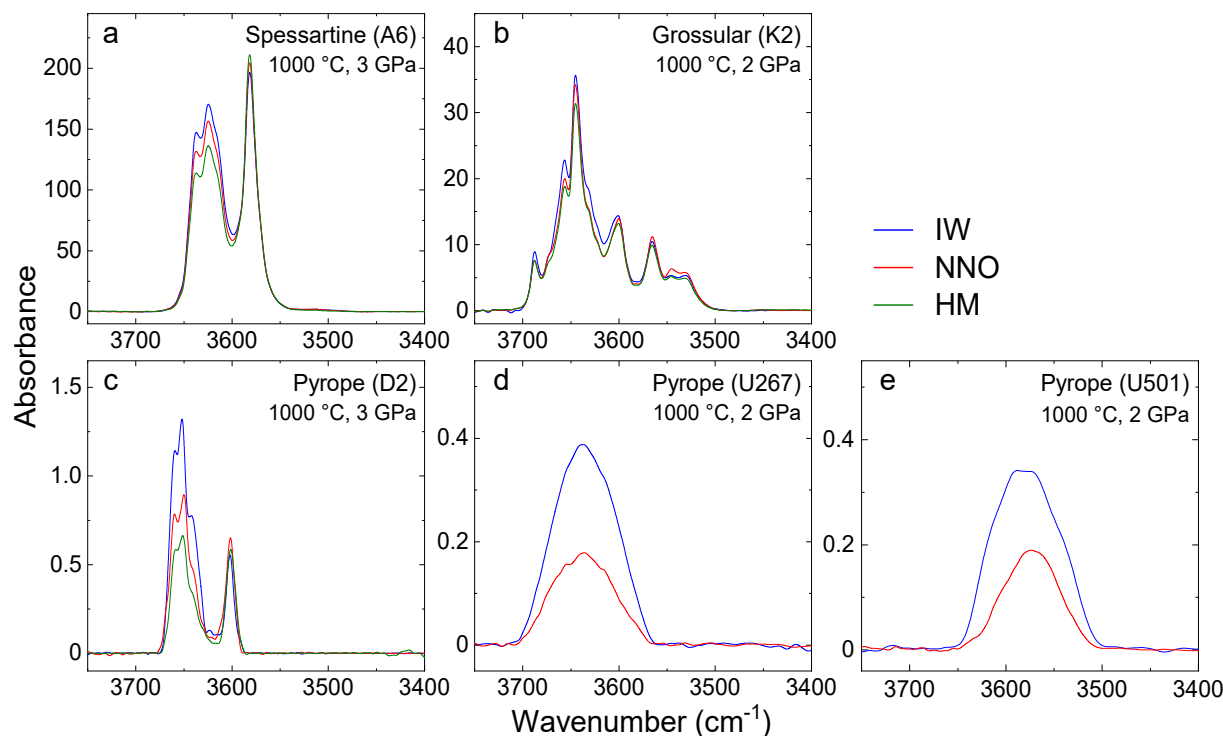


Figure 5. Representative Fourier-transform infrared (FTIR) spectra of annealed garnets. (a) Spessartine at 3 GPa and 1,000°C, (b) grossular at 2 GPa and 1,000°C, (c) pyrope (D2) at 3 GPa and 1,000°C, (d) pyrope (U267) at 2 GPa and 1,000°C, and (e) pyrope (U501) at 2 GPa and 1,000°C. Spectra were normalized to 1 cm thickness.

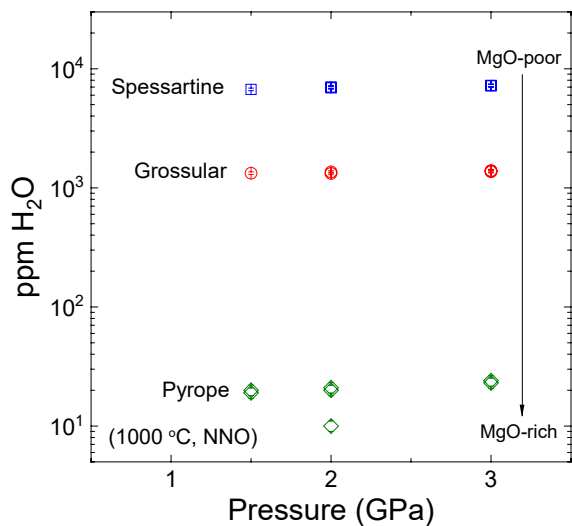


Figure 6. A comparison of OH content between different garnets annealed at 1,000°C and NNO. Error bars are 2% for spessartine and grossular and 7% for pyrope (see text).

(Aines & Rossman, 1984; Cohen-Addad et al., 1967; Lager et al., 1989; Rossman & Aines, 1991). Geiger and Rossman (2020a, 2020b) proposed that OH bands in garnets are mostly caused by OH clusters of different sizes, and other substitutions mechanisms are not required. This explains some high frequency bands at $>3,600\text{ cm}^{-1}$ in garnets, except those at $>3,670\text{ cm}^{-1}$ which are ascribed to tiny inclusions of hydrous minerals. However, the OH cluster model relies on assumed comparable shifts in the O-H bond frequencies by bonds in other nonadjacent tetrahedra, that is unjustified (Mosenfelder et al., 2021).

The strong OH bands at 3,650–3,600 and 3,600–3,550 cm^{-1} in spessartine (Figures 1 and 5) cannot be simply ascribed to the hydrogarnet model, as recognized early by Aines and Rossman (1984). Recently, Mosenfelder et al. (2021) suggested that garnet OH bands at $>3,600\text{ cm}^{-1}$ are related to coupled OH-F substitutions, especially in relatively F-rich grossular and spessartine and in Dora Maira pyrope. These bands are often insignificant in mantle garnets due to their low F contents. The small and sharp band at 3,688 cm^{-1} is only observed in grossular (Figures 1 and 5; see also Aines & Rossman, 1984). This band is common in our annealed unzoned grossular, and the run conditions are beyond the stability field of many altered phases. The band is unlikely due to tiny altered inclusions as argued by Geiger and Rossman (2020a, 2020b). Similar conclusion is drawn for natural grossular based on geological and spectroscopic reasons (Mosenfelder et al., 2021). This band may not be due to OH-F substitutions because it is absent in other F-rich garnet (e.g., spessartine). Likely, the band is linked to the extremely enriched Ca (32.6 wt. % CaO) in grossular, but a strong effect of Ca is unlikely due to the small band intensity (Figure 5). This explains the absence of the band in low-Ca mantle garnets. The contrasting OH bands

are likely due to different OH cluster sizes and configurations. The band at 3,688 cm^{-1} is likely due to tiny inclusions of hydrous minerals. The band at 3,650–3,600 cm^{-1} is likely due to coupled OH-F substitutions. The band at 3,600–3,550 cm^{-1} is likely due to OH clusters of different sizes and configurations.

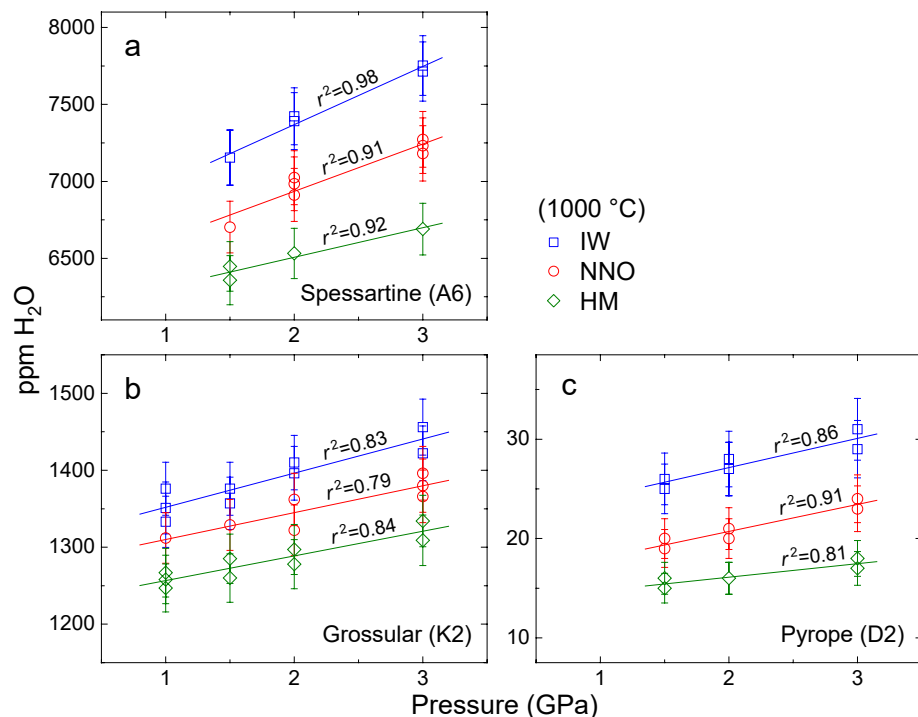


Figure 7. OH content of annealed garnets versus pressure at 1,000°C. (a) Spessartine, (b) grossular, and (c) pyrope. Different colors denote different $f\text{O}_2$ buffers. Solid lines are apparent best data fits. Error bars are 2% for spessartine and grossular and 7% pyrope (see text).

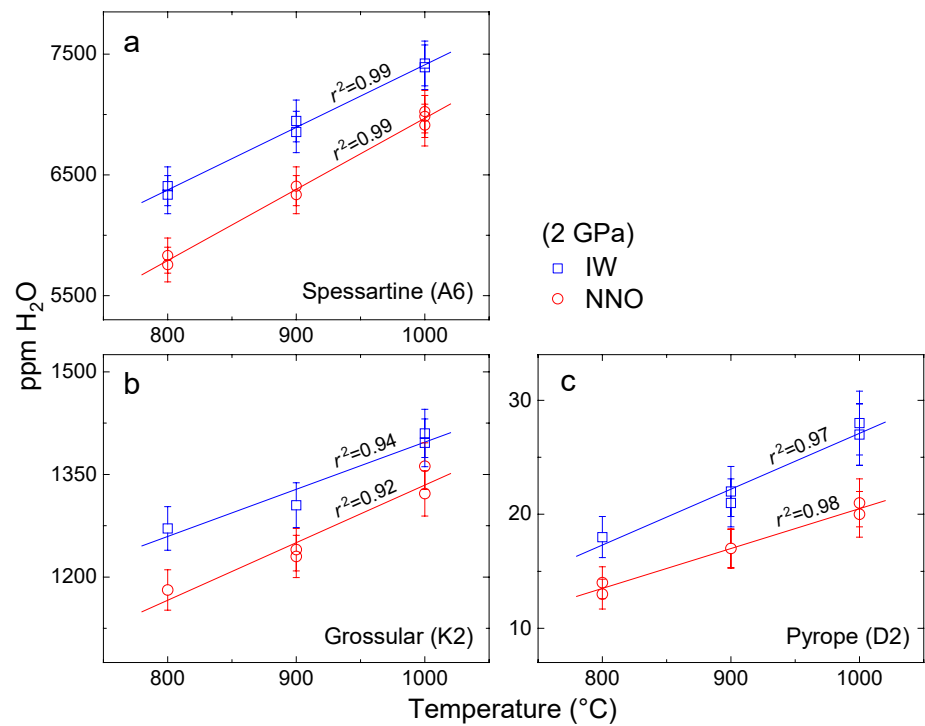


Figure 8. OH content of annealed garnets versus temperature at 2 GPa. (a) Spessartine, (b) grossular, and (c) pyrope. Solid lines are apparent best data fits. Error bars are 2% for spessartine and grossular and 7% pyrope (see text).

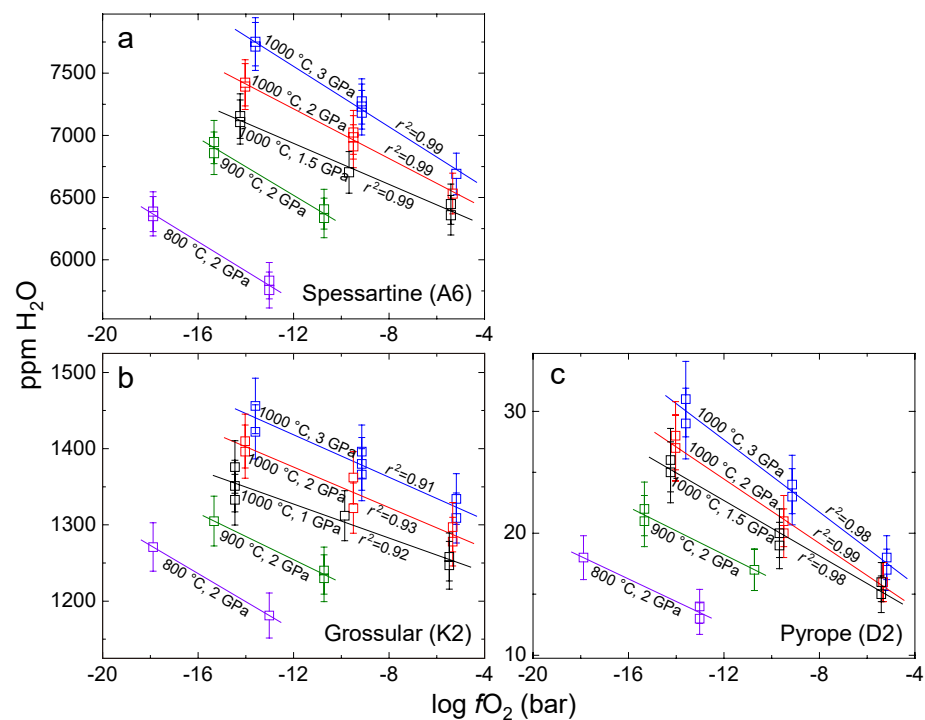


Figure 9. OH content of annealed garnets versus fO_2 . (a) Spessartine, (b) grossular, and (c) pyrope. Solid lines are apparent best data fits, and slopes are -82.5 to -121.5 in (a), -11.1 to -18.5 in (b), and -0.9 to -1.5 in (c). Data in runs with only two different oxygen buffer pairs were forced to fit with a linear relation, following the trends from runs with three different oxygen buffer pairs. Error bars are 2% for spessartine and grossular and 7% pyrope (see text).

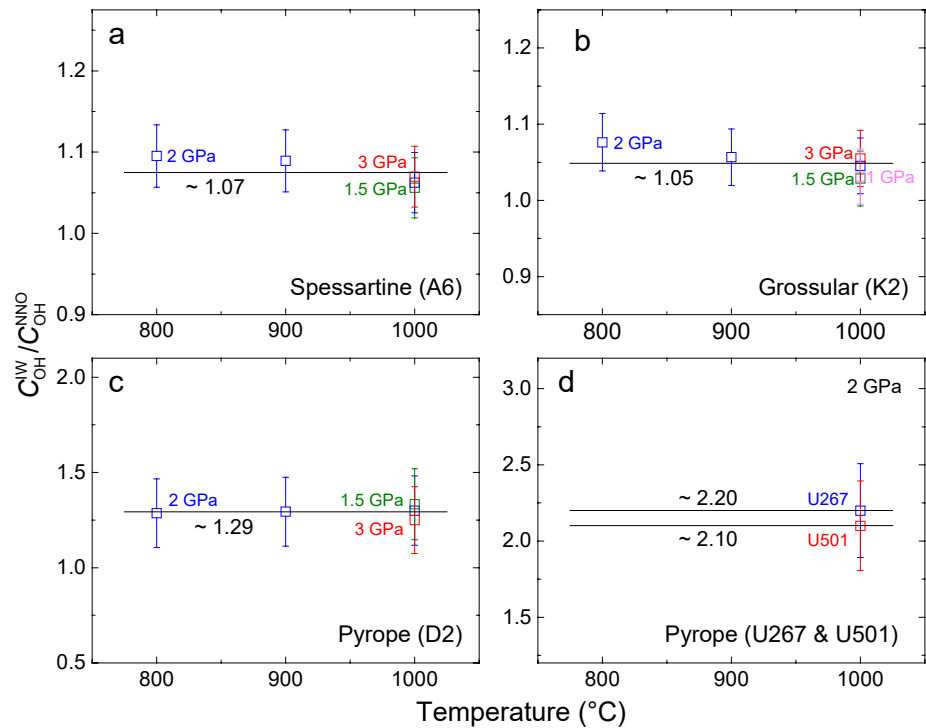


Figure 10. OH content ratio of runs buffered by IW and NNO. (a) Spessartine, (b) grossular, (c) pyrope (D2), and (d) pyrope (U267 and U501). Labels and symbols of the same pressure are marked by the same color in each panel. Solid lines in (a–c) are the average of all data for each garnet, and solid lines in (d) are ratios of two pyropes, following the data trends in (a–c) which suggest the ratio independent of pressure and temperature. Error bars are propagated from an assumed OH content uncertainty of 2% for spessartine and grossular and 7% for pyropes (see text).

in the three pyropes (Figures 1 and 5) may be caused by chemical differences between them and complex interactions between the atoms.

Because the starting garnets of different compositions can be broadly regarded as synthesized samples variably doped with major/minor elements (Section 2.1), the OH solubility at fixed sample chemistry allows to put constraints on the incorporation mechanism(s). At given pressure, temperature, and f_{O_2} , the OH solubility is significantly reduced with increasing MgO from spessartine to grossular to pyropes (Figure 6), for example, ~0.02, 0.55, and 18.6–26.4 wt. % MgO, respectively (Table 1). Thus, Mg may depress OH incorporation (especially for spessartine A6 and pyrope D2 showing less variation in other major/minor elements), although the exact mechanism is unclear. For the three pyropes, the OH solubility is comparable (10–30 ppm) at the run conditions, implying that the effect of MgO in the 18–26 wt. % range is similar and/or that the opposite FeO variation range of 4.5–8.5 wt. % counteracts the effect of MgO (the enhanced OH incorporation by Fe will be discussed below).

In general, our experimental studies suggest that the incorporation of OH in garnet is probably strongly affected by Si, Mg, and Fe in the structure, rather than by Si alone as often argued for the hydrogarnet cluster model. Multiple incorporation mechanisms of OH in garnet are highly likely to be simultaneously active. The content of other elements (Al, Cr and Ti) also varies in the garnet, but no evidence has been provided for their significant role in OH incorporation (Aines & Rossman, 1984; Geiger & Rossman, 2018, 2020a, 2020b; Mosenfelder et al., 2021; and this study).

6. Effects of f_{O_2} on OH Incorporation and Comparison With Other Minerals

For the three types of garnets, spessartine, grossular, and pyropes, the OH solubility at fixed sample chemistry commonly decreases from IW to NNO to HM at comparable conditions (Figure 9). At given pressure and temperature, the equilibrium water fugacity (f_{H_2O}) in the system increases with increasing f_{O_2} (Table 2). Therefore, the negative correlation between OH solubility and f_{O_2} in garnets is unlikely to be produced by the progressive

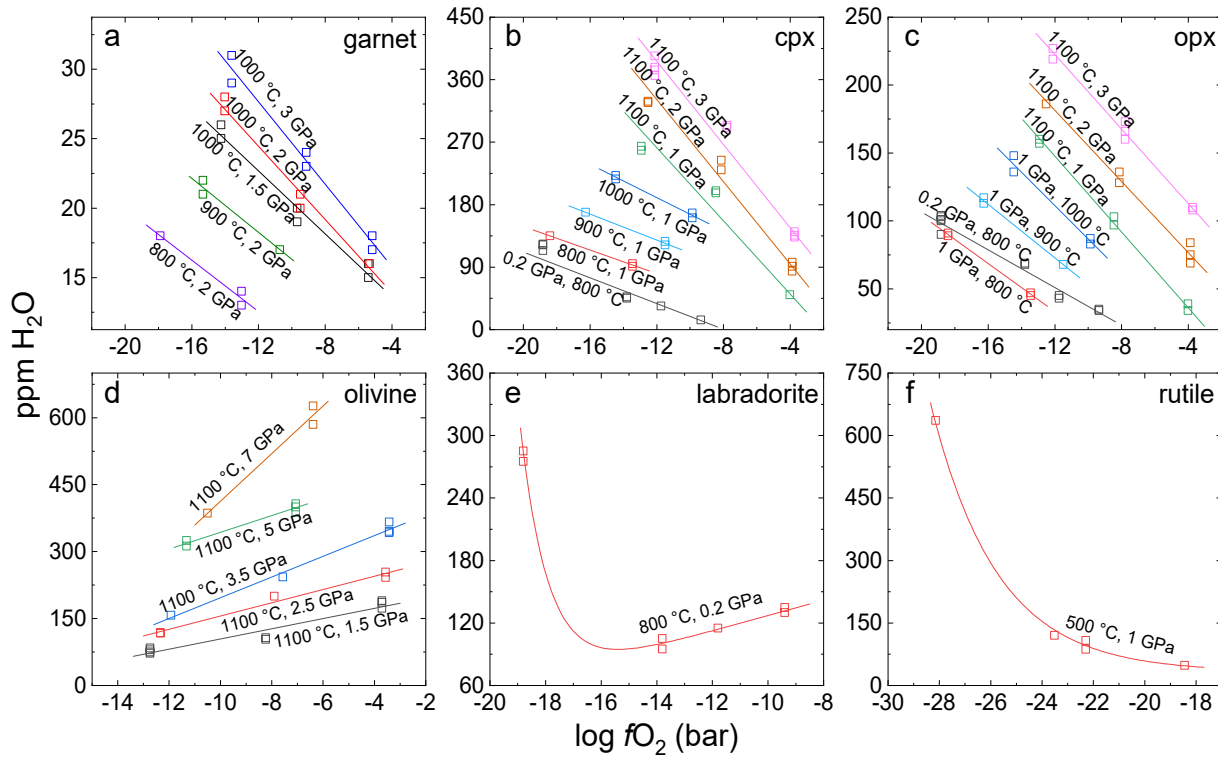
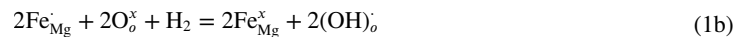


Figure 11. A comparison of fO_2 versus OH content between garnet and other minerals. (a) Garnet from this study (pyrope D2, solid lines are the same as in Figure 9, b) cpx, and (c) opx from Liu and Yang (2020), (d) olivine from Yang (2016), (e) labradorite from Yang (2012), and (f) rutile from Colasanti et al. (2011). Solid lines in (b–f) are apparent best fits from available studies.

increase of fH_2O from IW to NNO to HM, which would instead lead to a positive correlation between OH solubility and fH_2O as reported for olivine (Kohlstedt et al., 1996; Mosenfelder et al., 2006; Yang, 2015, 2016; Yang et al., 2014b). Under otherwise the same conditions, H_2 in the charge, as reflected by hydrogen fugacity (fH_2), becomes more abundant at more reduced conditions (Table 2). Therefore, the enhanced OH solubility in garnets could be related to:



where $H_{2\text{gas}}$ is produced by dissociation of H_2O , and Equation 1b is Equation 1a in the Kröger-Vink notation. This mechanism was applied to interpret the enhanced OH solubility in clinopyroxene (cpx) and orthopyroxene (opx) at IW relative to NNO (Bromiley et al., 2004; Liu & Yang, 2020; Rauch & Keppler, 2002). For Mn-rich spessartine, the Mn^{3+} to Mn^{2+} reduction may similarly enhance the OH dissolution, but this is unlikely to be important because the redox proxy of OH solubility, $C_{\text{OH}}^{\text{IW}}/C_{\text{OH}}^{\text{NNO}}$, is similar to that of Mn-poor grossular (Figure 10). Equation 1 does not imply that the OH incorporation in garnet is entirely related to the reduction of Fe^{3+} to Fe^{2+} , and that all the bands are linked to Fe. Instead, multiple mechanisms of OH incorporation are probably operative at the same time, for example, by substitutions involving Si, Mg, and Fe (and F in some garnets, Section 5). Therefore, Equation 1 only explains the negative correlation of OH solubility and fO_2 . The different slopes of OH solubility versus $\log fO_2$ (Figure 9) and the different $C_{\text{OH}}^{\text{IW}}/C_{\text{OH}}^{\text{NNO}}$ ratios (Figure 10) between different garnets are related to their Fe content (see details later).

The general negative correlation of OH solubility in garnet with fO_2 , using pyrope D2 as an example, is shown in Figure 11 for comparison with other nominally anhydrous minerals from the literature data including cpx (Liu & Yang, 2020), opx (Liu & Yang, 2020), olivine (Yang, 2016), labradorite (Yang, 2012), and rutile (Colasanti et al., 2011). With increasing fO_2 (on a log scale), the solubility decreases linearly in garnet (Figure 11a), cpx (Figure 11b), and opx (Figure 11c), but increases linearly in olivine (Figure 11d), decreases sharply first and then

increases slowly in labradorite (Figure 11e), and decreases nonlinearly in rutile (Figure 11f). For each of these minerals, the OH spectral shapes and patterns are the same over the run conditions, indicating the same mechanism(s) of OH incorporation. The different correlations of fO_2 and OH solubility between the minerals imply different mechanisms for the redox-controlled OH incorporation.

The negative OH solubility correlations for garnet, cpx, and opx can be explained by the reduction of Fe^{3+} to Fe^{2+} and the coupled OH incorporation (Equation 1). The OH bands in olivine are complex, and four OH incorporation modes have been proposed (Berry et al., 2005), namely protonation by Mg vacancies (3,300–3,100 cm^{-1} bands), trivalent cations (3,450–3,300 cm^{-1} bands), octahedral Ti (~3,572 and 3,525 cm^{-1} bands), and Si vacancies (3,650–3,450 cm^{-1} bands excluding the two Ti-related). The positive correlation for olivine can be caused by the coupled substitution of H plus Fe^{3+} for two Mg^{2+} and the increase in Fe^{3+} at more oxidized conditions (Yang, 2016). The inverted bell-shaped correlation for labradorite is hard to explain. At first sight, the enhanced solubility at very reduced conditions may be related to Fe, by Equation 1 as in garnet and pyroxenes. This is, however, unlikely to cause the positive trend under more oxidizing conditions. In particular, feldspars are usually poor in Fe, and some unknown mechanism may dominate the fO_2 -dependent OH incorporation (Mosenfelder et al., 2020; Yang, 2012). The negative nonlinear correlation for rutile is by the Ti^{4+} to Ti^{3+} reduction and the coupled incorporation of OH (Colasanti et al., 2011). Thus, fO_2 affects OH incorporation in nominally anhydrous minerals, either Fe-rich or poor, and the general effects differ between different minerals. Understanding the effects of fO_2 on OH solubility can provide new insights into the OH incorporation.

7. Coupled Effects of fO_2 and FeO and Geochemical Implications

The redox-related OH proxy, C_{OH}^{IW}/C_{OH}^{NNO} , is a factor determined only by the chemical composition (major and minor elements) of garnet (Figure 10), which affects OH solubility at high pressure and temperature. C_{OH}^{IW}/C_{OH}^{NNO} is sensitive to the garnet Fe content (expressed as total FeO, wt.%), and is greater at higher FeO (Figure 12). The documented effects of fO_2 on OH solubility are related to the redox-driven reactions of Fe^{3+} and Fe^{2+} and the accompanied OH incorporation. Therefore, the effects of fO_2 and FeO on OH solubility in garnet are coupled, as is well reflected by Equation 1. This implies that, if more Fe is present in the structure, the Fe^{3+} to Fe^{2+} reduction upon a fO_2 change requires the incorporation of a greater amount of OH to attain the equilibrium of Equation 1. This explains the small changes of the relative OH peak intensities in spessartine and grossular when fO_2 is modified (Figure 5), because they contain less FeO than the pyropes (Table 1). The apparent best data fit to C_{OH}^{IW}/C_{OH}^{NNO} and FeO content in the studied samples yields:

$$C_{OH}^{IW}/C_{OH}^{NNO} = A \times \exp\left(\frac{x}{t}\right) + y_0 \quad (2)$$

where A , t , and y_0 are constants of 0.03 ± 0.06 , 2.29 ± 1.19 , and 0.99 ± 0.14 , respectively, and x is the FeO content (wt. %). Equation 2 generally holds for the studied types of garnets, regardless of the origins and equilibrium pressure and temperature (Section 2.1 and Figure 10). It is at present unclear if Equation 2 is applicable to more Fe-rich (FeO > 10 wt. %) almandine garnets, yet it allows to model redox effects of OH in garnets from mantle peridotites that are mainly pyrope-rich, with 20–30% of grossular and almandine components (Wood et al., 2013). In fact, a worldwide data compilation gives a FeO range of 5.5–10.0 wt. % for garnets in mantle peridotites and defines no systematic variation with depth (50–250 km, Figure 13a).

Among the five garnets that were used in this study, two (pyrope U267 and U501) are from peridotite xenoliths, thus of mantle provenance (with preexisting point defects inherited from their mantle sources). The three pyropes (D2, U267, and U501) differ in composition, especially in Si, Mg, and Fe that greatly affect OH incorporation (Section 5); however, the solubility of OH in the annealed samples is rather similar, 10–30 ppm H_2O at 1.5–3 GPa, 800–1,000°C and NNO-IW (Table 3). These contents may not reflect the

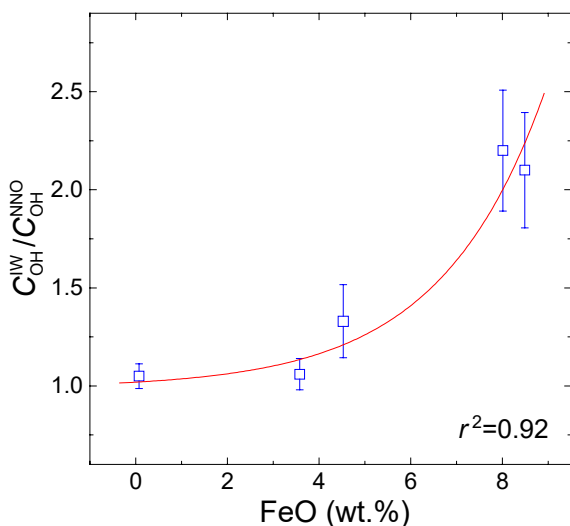


Figure 12. OH content ratio of runs buffered by IW and NNO versus FeO content (wt. %) in garnets. Data-points are average ratio for each type of garnet, which are independent of pressure and temperature (Figure 10). Error bars are propagated from an assumed water content uncertainty of 2% for spessartine and grossular and 7% for pyropes (see text). Data are best fitted with an exponential relation (Equation 2).

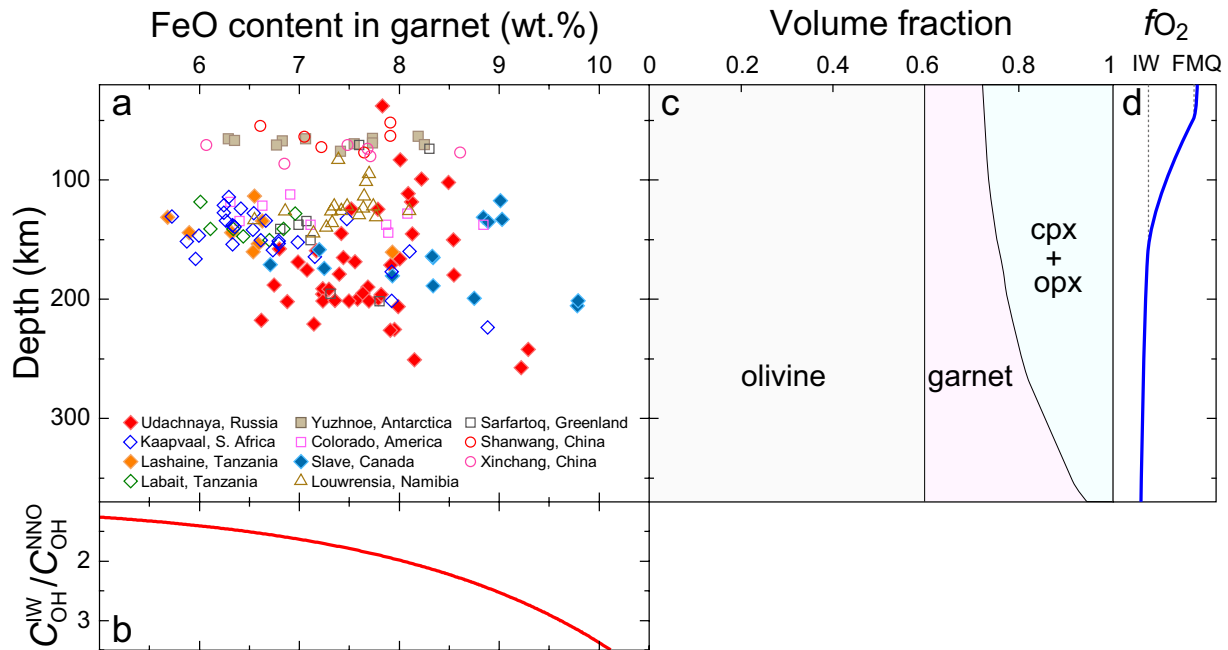


Figure 13. FeO content of mantle garnets and variations of C_{OH}^{IW}/C_{OH}^{NNO} , mineral volume and redox state. FeO contents in (a) are from reported data of garnets in peridotite xenoliths, thick curve in (b) is plotted with Equation 2, modal mineral composition in (c) is after Frost (2008), and redox trend in (d) shows the fO_2 change after Frost and McCammon (2008), Rohrbach and Schmidt (2011), and Stagno et al. (2013). The significant range of garnet FeO content with depth contrasts sharply to the very limited (relative) variation of SiO_2 and MgO (Appendix), favoring the application of the experimental results to the mantle (see text). Data sources of garnet peridotites: Udachnaya, Russia (Doucet et al., 2013; Ionov et al., 2010; Yaxley et al., 2012); Vitim, Russia (Ionov et al., 2005); Kaapvaal, S. Africa (Boyd et al., 1993; Canil & O'Neill, 1996); Lashaine, Tanzania (Henjes-kunst & Alterr, 1992; Rudnick, 1994); Labait, Tanzania (Lee & Rudnick, 1999); Slave, Canada (Kopylova et al., 1999); Louwrensia, Namibia (Boyd et al., 2004); Yuzhnoe, Antarctic (Foley et al., 2006); Colorado, America (Li et al., 2008; Smith et al., 1991); Sarfartoq, Greenland (Bizzarro & Stevenson, 2003); Shanwang, China (Zheng et al., 2006); Xinchang, China (Liu et al., 2012).

true OH solubility at the corresponding conditions, because the equilibrium of major and minor elements under the studied conditions is not strictly considered (Tollan et al., 2018). In principle, the equilibrium content of OH in a mineral grown from well mixed reagents in a hydrous melt may be more meaningful in defining the solubility at the conditions of interest (Section 2.1). However, experimental studies have shown that, over a wide range of pressure under otherwise similar conditions (including chemistry), the solubility data of OH in a mineral by annealing a natural crystal with a hydrous fluid are generally consistent with those in the synthetic mode systems, for example, for opx (Rauch & Keppler, 2002). Moreover, chemical analyses of garnet in mantle peridotite xenoliths demonstrate that, for the three elements Si, Mg, and Fe (dominating OH incorporation), the relative variation of SiO_2 (41.7 ± 1.0 wt. %) and MgO (20.8 ± 1.8 wt. %) with depth are both small, mostly within $\pm 5\%$ (Appendix), when compared to that of FeO (7.5 ± 2 wt. %, i.e., $\sim 30\%$ relative, Figure 13a). Therefore, the broadly comparable and similarly low OH solubility in the three pyropes, especially in the two peridotite pyropes, suggests that the storage capacity of OH in mantle garnet is generally small. In this case, garnet is unlikely to be a major water carrier in the mantle. This is consistent with the reported very low OH contents of garnet in mantle peridotite xenoliths, mostly 0–20 ppm H_2O (Doucet et al., 2014; Matsyuk et al., 1998).

Furthermore, the results of this study also offer critical information on partitioning of OH between garnet and olivine, two major constituents in the deep upper mantle. The C_{OH}^{IW}/C_{OH}^{NNO} estimated with Equation 2 for the FeO range of mantle garnets (Figure 13a) is from 1.5 to 2.5 (Figure 13b), such that the capacity of garnet to structurally accommodate OH is 50–150% greater at reduced (IW) than at oxidized (NNO) conditions. By contrast, the OH solubility in olivine is greater under more oxidized conditions (Figure 11). At comparable conditions in the mantle, for example, 50–250 km depth range, the C_{OH}^{IW}/C_{OH}^{NNO} ratio is $\sim 50\%$ smaller at IW than at NNO in olivine (Yang, 2016), but is 50–150% greater in garnet (Figure 13). Hence, the partition coefficient of OH between garnet and olivine is fO_2 -dependent. It is smaller in more oxidized mantle and greater in more reduced mantle, and thus is unlikely to be constant in the upper mantle. This explains, at least partly, the highly variable OH partition

coefficients between garnet and olivine in Udachnaya peridotites, from 0.01 to 0.2, assuming the preservation of initial water contents in the minerals (Doucet et al., 2014).

Data Availability Statement

The authors comply with FAIR Data guidelines, and the data are available in the general repository, Zenodo (<https://doi.org/10.5281/zenodo.6360671>).

Acknowledgments

X.Y. thanks Hans Keppler for helpful discussion and Charles Geiger for supplying the starting Dora Maira pyrope. Comments by Jörg Hermann and anonymous reviewers helped to improve the manuscript. This work was supported by National Science Foundation of China (41725008) to X.Y. and Chinese Academy of Sciences President's International Fellowship Initiative (2017VCA0009) to D.I.

References

- Ackermann, L., Cemič, L., & Langer, K. (1983). Hydrogarnet substitution in pyrope: A possible location for “water” in the mantle. *Earth and Planetary Science Letters*, *62*, 208–214.
- Aines, R. D., & Rossman, G. R. (1984). The hydrous component in garnets: Pyralites. *American Mineralogist*, *69*, 1116–1126.
- Ardia, P., Hirschmann, M. M., Withers, A. C., & Tenner, T. J. (2012). H₂O storage capacity of olivine at 5–8 GPa and consequences for dehydration partial melting of the upper mantle. *Earth and Planetary Science Letters*, *345–348*, 104–116.
- Bai, Q., & Kohlstedt, D. L. (1993). Effects of chemical environment on the solubility and incorporation mechanism for hydrogen in olivine. *Physics and Chemistry of Minerals*, *19*, 460–471.
- Behrens, H. (2021). Hydrogen defects in feldspars: Defect properties and implications for water solubility in feldspar. *Physics and Chemistry of Minerals*, *48*, 1–22.
- Bell, D. R., Ihinger, P. D., & Rossman, G. R. (1995). Quantitative analysis of trace OH in garnet and pyroxenes. *American Mineralogist*, *80*, 465–474.
- Bell, D. R., & Rossman, G. R. (1992). Water in Earth's mantle: The role of nominally anhydrous minerals. *Science*, *255*, 1391–1397.
- Bell, D. R., Rossman, G. R., & Moore, R. O. (2004). Abundance and partitioning of OH in a high-pressure magmatic system: Megacrysts from the Monastery kimberlite, South Africa. *Journal of Petrology*, *45*, 1539–1564.
- Berry, A. J., Hermann, J., O'Neill, H. S. C., & Foran, G. J. (2005). Fingerprinting the water site in mantle olivine. *Geology*, *33*, 869–872.
- Bizzarro, M., & Stevenson, R. K. (2003). Major element composition of the lithospheric mantle under the North Atlantic craton: Evidence from peridotite xenoliths of the Sarfartoq area, southwestern Greenland. *Contributions to Mineralogy and Petrology*, *146*, 223–240.
- Boyd, F. R., Pearson, D. G., Hoal, K. O., Hoal, B. G., Nixon, P. H., Kingston, M. J., & Mertzman, S. A. (2004). Garnet lherzolites from Louwrensia, Namibia: Bulk composition and P/T relations. *Lithos*, *77*, 573–592.
- Boyd, F. R., Pearson, D. G., Nixon, P. H., & Mertzman, S. A. (1993). Low-calcium garnet harzburgites from southern Africa: Their relations to craton structure and diamond crystallization. *Contributions to Mineralogy and Petrology*, *113*, 352–366.
- Bromiley, G. D., Keppler, H., McCammon, C., Bromiley, F. A., & Jacobsen, S. D. (2004). Hydrogen solubility and speciation in natural, gem-quality chromian diopside. *American Mineralogist*, *89*, 941–949.
- Canil, D., & O'Neill, H. S. C. (1996). Distribution of ferric iron in some upper-mantle assemblages. *Journal of Petrology*, *37*, 609–635.
- Cohen-Addad, C., Ducros, P., & Bertaut, E. F. (1967). Étude de la substitution du groupement SiO₄ par (OH)₄ dans les composés Al₂Ca₃(OH)₁₂ et Al₂Ca₃(SiO₄)_{2,16}(OH)_{3,36} de type grenat. *Acta Crystallographica*, *23*, 220–230.
- Colasanti, C. V., Johnson, E. A., & Manning, C. E. (2011). An experimental study of OH solubility in rutile at 500–900°C, 0.5–2 GPa, and a range of oxygen fugacities. *American Mineralogist*, *96*, 1291–1299.
- Doucet, L. S., Ionov, D. A., & Golovin, A. V. (2013). The origin of coarse garnet peridotites in cratonic lithosphere: New data on xenoliths from the Udachnaya kimberlite, central Siberia. *Contributions to Mineralogy and Petrology*, *165*, 1225–1242.
- Doucet, L. S., Peslier, A. H., Ionov, D., Brandon, A. D., Golovin, A. V., Goncharov, A. G., & Ashchepkov, I. V. (2014). High water contents in the Siberian cratonic mantle linked to metasomatism: An FTIR study of Udachnaya peridotite xenoliths. *Geochimica et Cosmochimica Acta*, *137*, 159–187.
- Foley, S. F., Andronikov, A. V., Jacob, D. E., & Melzer, S. (2006). Evidence from Antarctic mantle peridotite xenoliths for changes in mineralogy, geochemistry and geothermal gradients beneath a developing rift. *Geochimica et Cosmochimica Acta*, *70*, 3096–3120.
- Frost, B. R. (1991). Introduction to oxygen fugacity and its petrological importance. *Reviews in Mineralogy and Geochemistry*, *25*, 1–9.
- Frost, D. J. (2008). The upper mantle and transition zone. *Elements*, *4*, 171–176.
- Frost, D. J., & McCammon, C. A. (2008). The redox state of Earth's mantle. *Annual Review of Earth and Planetary Sciences*, *36*, 389–420.
- Geiger, C. A., & Rossman, G. R. (2018). IR spectroscopy and OH– in silicate garnet: The long quest to document the hydrogarnet substitution. *American Mineralogist: Journal of Earth and Planetary Materials*, *103*, 384–393.
- Geiger, C. A., & Rossman, G. R. (2020a). Micro- and nano-size hydrogarnet clusters and proton ordering in calcium silicate garnet. Part I: The quest to understand the nature of “water” in garnet continues. *American Mineralogist: Journal of Earth and Planetary Materials*, *105*, 455–467.
- Geiger, C. A., & Rossman, G. R. (2020b). Micro- and nano-size hydrogarnet clusters in calcium silicate garnet. Part II: Mineralogical, petrological, and geochemical aspects. *American Mineralogist: Journal of Earth and Planetary Materials*, *105*, 468–478.
- Goncharov, A. G., Ionov, D. A., Doucet, L. S., & Pokhilenko, L. N. (2012). Thermal state, oxygen fugacity and C–O–H fluid speciation in cratonic lithospheric mantle: New data on peridotite xenoliths from the Udachnaya kimberlite, Siberia. *Earth and Planetary Science Letters*, *357*, 99–110.
- Henjes-kunst, F., & Alterr, R. (1992). Metamorphic petrology of xenoliths from Kenya and northern Tanzania and implications for geotherms and lithospheric structures. *Journal of Petrology*, *33*, 1125–1156.
- Herd, C. D. K. (2008). Basalts as probes of planetary interior redox state. *Reviews in Mineralogy and Geochemistry*, *68*, 527–554.
- Ingrin, J., & Blanchard, M. (2006). Diffusion of hydrogen in minerals. In H. Keppler & J. R. Smyth (Eds.), *Water in nominally anhydrous minerals* (Vol. 62, pp. 291–320). Washington, DC: Mineralogical Society of America.
- Ionov, D. A., Ashchepkov, I., & Jagoutz, E. (2005). The provenance of fertile off-craton lithospheric mantle: Sr–Nd isotope and chemical composition of garnet and spinel peridotite xenoliths from Vitim, Siberia. *Chemical Geology*, *217*, 41–75.
- Ionov, D. A., Doucet, L. S., & Ashchepkov, I. V. (2010). Composition of the lithospheric mantle in the Siberian craton: New constraints from fresh peridotites in the Udachnaya-East kimberlite. *Journal of Petrology*, *51*, 2177–2210.
- Kohlstedt, D. L., Keppler, H., & Rubie, D. C. (1996). Solubility of water in the α , β , and γ phases of (Mg,Fe)₂SiO₄. *Contributions to Mineralogy and Petrology*, *123*, 345–357.

- Kopylova, M. G., Russell, J. K., & Cookenboo, H. (1999). Petrology of peridotite and pyroxenite xenoliths from the Jericho kimberlite: Implications for the thermal state of the mantle beneath the Slave craton, northern Canada. *Journal of Petrology*, *40*, 79–104.
- Lager, G. A., Armbruster, T., Rotella, F. J., & Rossman, G. R. (1989). OH substitution in garnets: X-Ray and neutron diffraction, infrared, and geometric-modeling studies. *American Mineralogist*, *74*, 840–851.
- Langer, K., Robarick, E., Sobolev, N. V., Shatsky, V. S., & Wang, W. (1993). Single-crystal spectra of garnets from diamondiferous high-pressure metamorphic rocks from Kazakhstan: Indications for OH⁻, H₂O, and FeTi charge transfer. *European Journal of Mineralogy*, *5*, 1091–1100.
- Lee, C. T., & Rudnick, R. L. (1999). Compositionally stratified cratonic lithosphere: Petrology and geochemistry of peridotite xenoliths from the Labait tuff cone, Tanzania. In *Proceedings of the 7th international Kimberlite conference* (pp. 503–521). Cape Town: Red Roof Design.
- Li, Z. X., Lee, C. T., Peslier, A. H., Lenardic, A., & Mackwell, S. J. (2008). Water contents in mantle xenoliths from the Colorado Plateau and vicinity: Implications for the mantle rheology and hydration-induced thinning of continental lithosphere. *Journal of Geophysical Research*, *113*, B09210. <https://doi.org/10.1029/2007JB005540>
- Liu, C.-Z., Wu, F.-Y., Sun, J., Chu, Z.-Y., & Qiu, Z.-L. (2012). The Xinchang peridotite xenoliths reveal mantle replacement and accretion in southeastern China. *Lithos*, *150*, 171–187.
- Liu, H., & Yang, X. (2020). Solubility of hydroxyl groups in pyroxenes: Effect of oxygen fugacity at 0.2–3 GPa and 800–1200°C. *Geochimica et Cosmochimica Acta*, *286*, 355–379.
- Lu, R., & Keppler, H. (1997). Water solubility in pyrope to 100 kbar. *Contributions to Mineralogy and Petrology*, *129*, 35–42.
- Maldener, J., Hosch, A., Langer, K., & Rauch, F. (2003). Hydrogen in some natural garnets studied by nuclear reaction analysis and vibrational spectroscopy. *Physics and Chemistry of Minerals*, *30*, 337–344.
- Matsyuk, S., Langer, K., & Hosch, A. (1998). Hydroxyl defects in garnets from mantle xenoliths in kimberlites of the Siberian platform. *Contributions to Mineralogy and Petrology*, *132*, 163–179.
- Mookherjee, M., & Karato, S. (2010). Solubility of water in pyrope-rich garnet at high pressures and temperature. *Geophysical Research Letters*, *37*, L03310. <https://doi.org/10.1029/2009GL041289>
- Mosenfelder, J. L., Andrys, J. L., von der Handt, A., Kohlstedt, D. L., & Hirschmann, M. M. (2020). Hydrogen incorporation in plagioclase. *Geochimica et Cosmochimica Acta*, *277*, 87–110.
- Mosenfelder, J. L., Deligne, N. I., Asimow, P. D., & Rossman, G. R. (2006). Hydrogen incorporation in olivine from 2–12 GPa. *American Mineralogist*, *91*, 285–294.
- Mosenfelder, J. L., von der Handt, A., Withers, A. C., Bureau, H., Raepsaet, C., & Rossman, G. R. (2021). Coupled hydrogen and fluorine incorporation in garnet: New constraints from FTIR, ERDA, SIMS and EPMA. *American Mineralogist*, *98*(5–6), 1042–1054. <https://doi.org/10.2138/am-2021-7880>
- Rauch, M., & Keppler, H. (2002). Water solubility in orthopyroxene. *Contributions to Mineralogy and Petrology*, *143*, 525–536.
- Reynes, J., Jollands, M., Hermann, J., & Ireland, T. (2018). Experimental constraints on hydrogen diffusion in garnet. *Contributions to Mineralogy and Petrology*, *173*, 69. <https://doi.org/10.1007/s00410-018-1492-z>
- Robie, R. A., & Hemingway, B. S. (1995). *Thermodynamic properties of minerals and related substances at 298.15 K and 1 bar (10⁵ Pascals) pressure and at higher temperatures*. Washington, DC: United States Government Printing Office.
- Rohrbach, A., & Schmidt, M. W. (2011). Redox freezing and melting in the Earth's deep mantle resulting from carbon–iron redox coupling. *Nature*, *472*, 209–212.
- Rossman, G. R., & Aines, R. D. (1991). The hydrous components in garnets: Grossular-hydrogrossular. *American Mineralogist*, *76*, 1153–1164.
- Rudnick, R. L. (1994). Northern Tanzanian peridotite xenolith: A comparison with Kaapvaal peridotites and evidence for carbonatite interaction with ultra-refractory residues. In *Proceedings of the fifth International kimberlite conference* (pp. 336–353). CPRM.
- Sheng, Y. M., Xia, Q. K., Dallai, L., Yang, X., & Hao, Y. T. (2007). H₂O contents and D/H ratios of nominally anhydrous minerals from ultra-high-pressure eclogites of the Dabie orogen, eastern China. *Geochimica et Cosmochimica Acta*, *71*, 2079–2103.
- Smith, D., Griffin, W. L., Ryan, C. G., & Sie, S. H. (1991). Trace-element zonation in garnets from the Thumb: Heating and melt infiltration below the Colorado plateau. *Contributions to Mineralogy and Petrology*, *107*, 60–79.
- Stagno, V., Ojwang, D. O., McCammon, C. A., & Frost, D. J. (2013). The oxidation state of the mantle and the extraction of carbon from Earth's interior. *Nature*, *493*, 84–88.
- Stalder, R., Potrafke, A., Billström, K., Skogby, H., Meinhold, G., Gögele, C., & Berberich, T. (2017). OH defects in quartz as monitor for igneous, metamorphic, and sedimentary processes. *American Mineralogist*, *102*, 1832–1842.
- Tollan, P., O'Neill, H., & Hermann, J. (2018). The role of trace elements in controlling H incorporation in San Carlos olivine. *Contributions to Mineralogy and Petrology*, *173*, 89. <https://doi.org/10.1007/s00410-018-1517-7>
- Withers, A. C., Wood, B. J., & Carroll, M. R. (1998). The OH content of pyrope at high pressure. *Chemical Geology*, *147*, 161–171.
- Wood, B. J., Bryndzia, L. T., & Johnson, K. E. (1990). Mantle oxidation state and its relationship to tectonic environment and fluid speciation. *Science*, *248*, 337–345.
- Wood, B. J., Kiseeva, E. S., & Matzen, A. K. (2013). Garnet in the Earth's mantle. *Elements*, *9*, 421–426.
- Xia, Q. K., Sheng, Y. M., & Yang, X. (2005). Heterogeneity of water in garnets from UHP eclogites, eastern Dabieshan, China. *Chemical Geology*, *224*, 237–246.
- Yang, X. (2012). An experimental study of H solubility in feldspars: Effect of composition, oxygen fugacity, temperature and pressure and implications for crustal processes. *Geochimica et Cosmochimica Acta*, *97*, 46–57.
- Yang, X. (2015). OH solubility in olivine in the peridotite-COH system under reducing conditions and implications for water storage and hydrous melting in the reducing upper mantle. *Earth and Planetary Science Letters*, *432*, 199–209.
- Yang, X. (2016). Effect of oxygen fugacity on OH dissolution in olivine under peridotite-saturated conditions: An experimental study at 1.5–7 GPa and 1100–1300°C. *Geochimica et Cosmochimica Acta*, *173*, 319–336.
- Yang, X., Gaillard, F., & Scaillot, B. (2014). A relatively reduced Hadean continental crust and implications for the early atmosphere and crustal rheology. *Earth and Planetary Science Letters*, *393*, 210–219.
- Yang, X., & Keppler, H. (2011). In-situ infrared spectra of OH in olivine to 1100°C. *American Mineralogist*, *96*, 451–454.
- Yang, X., Keppler, H., & Li, Y. (2016). Molecular hydrogen in mantle minerals. *Geochemical Perspectives Letters*, *2*, 160–168.
- Yang, X., Liu, D., & Xia, Q. (2014). CO₂-induced small water solubility in olivine and implications for properties of the shallow mantle. *Earth and Planetary Science Letters*, *403*, 37–47.
- Yaxley, G. M., Berry, A. J., Kamenetsky, V. S., Woodland, A. B., & Golovin, A. V. (2012). An oxygen fugacity profile through the Siberian Craton—Fe K-edge XANES determinations of Fe³⁺/ΣFe in garnets in peridotite xenoliths from the Udachnaya East kimberlite. *Lithos*, *140*, 142–151.
- Zhang, C., & Duan, Z. (2009). A model for C–O–H fluid in the Earth's mantle. *Geochimica et Cosmochimica Acta*, *73*, 2089–2102.

- Zhao, Y. H., Ginsberg, S. B., & Kohlstedt, D. L. (2004). Solubility of hydrogen in olivine: Dependence on temperature and iron content. *Contributions to Mineralogy and Petrology*, *147*, 155–161.
- Zheng, J. P., Griffin, W. L., O'Reilly, S. Y., Yang, J. S., Li, T. F., Zhang, M., et al. (2006). Mineral chemistry of peridotites from Paleozoic, Mesozoic and Cenozoic lithosphere: Constraints on mantle evolution beneath eastern China. *Journal of Petrology*, *47*, 2233–2256.